Physics of Fluids ARTICLE pubs.aip.org/aip/pof

Effect of boundary conditions on energy harvesting of a flow-induced snapping sheet at low Reynolds number

Cite as: Phys. Fluids **35**, 127103 (2023); doi: 10.1063/5.0171294
Submitted: 8 August 2023 · Accepted: 8 November 2023 ·
Published Online: 4 December 2023

Zhaokun Wang (王兆坤),[1,2,3] Fuwang Zhao (赵福旺),[1,2,3] Bowen Xu (徐博闻),[4] Lingwei Zeng (曾令伟),[1,a)] and Hui Tang (唐辉)[1,3,a)]

AFFILIATIONS

[1]Department of Mechanical Engineering, The Hong Kong Polytechnic University, Kowloon, Hong Kong, China
[2]School of Fashion and Textiles, The Hong Kong Polytechnic University, Kowloon, Hong Kong, China
[3]The Hong Kong Polytechnic University Shenzhen Research Institute, Shenzhen, Guangdong 518057, China
[4]School of Mechanical and Aerospace Engineering, Nanyang Technological University, Singapore 639798, Singapore

[a)]**Authors to whom correspondence should be addressed:** lingwei.zeng@connect.polyu.hk; h.tang@polyu.edu.hk

ABSTRACT

Recent studies on the snap-through motion of elastic sheets have attracted intense interest in energy-harvesting applications. However, the effect of boundary conditions (BCs) on energy extraction performance still remains an open question. In this study, we explored the snapping dynamics and energy-harvesting characteristics of the buckled sheet at various conditions using fluid–structure interaction simulations at a Reynolds number $Re = 100$. It was found that the front boundary condition (BC) dramatically affects the sheet's snapping dynamics, e.g., the pinned or relatively soft front BC triggers the sheet's instability easily and thus boasts the collection of potential energy. In the snap-through oscillation state, a stiffer rear BC results in a larger improvement in the sheet's energy collection compared with a minor effect of front BC. Meanwhile, the enhancement can also be achieved by adjusting the rear rotational spring stiffness up to 1.125×10^{-4}, after which it remains nearly constant, as observed in the case of $EI^* = 0.004$. This introduction of an elastic BC with $k_{rs}^* = 1.125 \times 10^{-4}$ not only efficiently enhances energy extraction but significantly reduces stress concentration and, as a result, greatly prolongs the sheet's fatigue durability, especially for the stiffer sheet with $EI^* = 0.004$. The effect of three other governing parameters, including the length ratio ΔL^*, sheet's bending stiffness EI^*, and mass ratio m^*, on the sheet's energy-harvesting performance were also explored. The result shows that increasing ΔL^* and EI^* could improve the total energy harvested, primarily by enhancing the elastic potential energy, particularly in the aft half of the sheet. In contrast, increasing m^* mainly enhances the kinetic energy collected by the sheet's central portion, thus improving the total energy-extracting performance. This study provides an in-depth insight into the dynamics of a buckled sheet under various BCs, which may offer some guidance on the optimization of relevant energy harvesters.

NOMENCLATURE

c_s	Sound speed
c_α	Lattice speed
E_{dk}	Instantaneous distributed kinetic energy
E_{dp}	Instantaneous distributed potential energy
E_k	Instantaneous kinetic energy
E_p	Instantaneous potential energy
$\bar{E}_{dp}$	Time-averaged distributed potential energy
$\bar{E}_{dk}$	Time-averaged distributed kinetic energy
$\bar{E}_k$	Time-averaged kinetic energy
$\bar{E}_p$	Time-averaged potential energy
E_{dk}^*	Non-dimensional instantaneous distributed kinetic energy
E_{dp}^*	Non-dimensional instantaneous distributed potential energy
E_k^*	Non-dimensional instantaneous kinetic energy
E_p^*	Non-dimensional instantaneous potential energy
$\bar{E}_{dk}^*$	Non-dimensional time-averaged distributed kinetic energy
$\bar{E}_{dp}^*$	Non-dimensional time-averaged distributed potential energy
$\bar{E}_k^*$	Non-dimensional time-averaged kinetic energy
$\bar{E}_p^*$	Non-dimensional time-averaged potential energy
EA	Stretching stiffness of the sheet

EA^*	Non-dimensional stretching stiffness of the sheet
EI	Bending stiffness of the sheet
EI^*	Non-dimensional bending stiffness of the sheet
F_f	External fluid loading acting on the sheet
f_e	Body force acting on the fluid
f_α	Particle density distribution function
f_α^{eq}	Equilibrium distribution function
L	Sheet length
ΔL	The compression of the sheet
ΔL^*	The compression ratio of the sheet
M	Transformation matrix
m^*	Non-dimensional mass ratio
p	Fluid pressure
p^*	Non-dimensional fluid pressure
Re	Reynolds number
S	Relaxation matrix
s^*	Non-dimensional Lagrangian coordinate along the sheet
T	Typical time period
t^*	Non-dimensional time
T_f	Flapping period
T_f^*	Non-dimensional flapping period
u	Fluid velocity
u^*	Non-dimensional fluid velocity
w_α	LBM lattice weighting
X	Position vector of the sheet
y_m^*	Vertical position of the sheet's middle point

Greek symbols

κ	Curvature
κ^*	Non-dimensional curvature
ν	Fluid kinematic viscosity
ρ_f	Fluid density
ρ_{f0}	Mean mass density
ρ_s	Linear density of the sheet

I. INTRODUCTION

Due to a rapid depletion of fossil fuel resources and a dramatic increase in carbon emissions, clean/blue energy is urgently required as an alternative energy source.[1–4] As a way to combat the energy crisis and environmental concerns, energy harvesting from ambient environment has emerged as an inexorably crucial means.[5–15] Bluff bodies (rigid or flexible) are frequently encountered in engineering applications, such as high-rise buildings, cooling towers, airfoils, etc.[16–22] Recently, energy harvesting through flow-induced vibration (FIV) of bluff bodies has attracted significant attention due to its abundant resources and environmental advantages, as reviewed by many prior studies.[13,23–26] These bluff body-based energy harvesters are usually subjected to crossflows, with the majority of them considering the uniform oncoming flow condition. Among them, an interesting one is harvesting energy from the flapping foils.[20,27–35]

Early studies were primarily concentrated on improving the energy-harvesting efficiency of rigid foil by altering the activation modes, such as fully active mode, fully passive or semi-active modes, and optimizing its kinematics.[31,33,36] In addition to that, the effect of foil's flexibility on energy-harvesting performance was also studied by introducing a flexible tail, a deformable head, or body, and their results demonstrate the benefits of flexibility on the improvement of energy extraction.[28,32,37–40] Recently, an innovative concept was proposed to broaden the resonance range and improve the energy-harvesting efficiency by triggering the snap-through phenomenon.[41–47] Snap-through represents a rapid shift of the system from one equilibrium state to another, accompanied by the conversion between kinetic and potential energies. The snapping-based harvesters can vibrate stably and periodically in a broader vibration regime from a low cut-in speed, overcoming the small operation range of vortex-induced vibration (VIV), chaotic oscillation of flutter, and high cut-in speed of galloping in conventional energy collectors. Additionally, in the snap-through systems, the pre-stored potential energy activates a sizeable flapping amplitude during snapping oscillations, considerably enhancing energy-harvesting efficiency. Qin *et al.*[44] experimentally investigated the energy-harvesting performance of a bistable piezoelectric energy generator. They found that, with the onset of snap-through in both VIV and galloping regimes, a high electricity output is achieved throughout a broader flow speed range, consistently maintaining an impressive vibration amplitude to produce power. Badhurshah *et al.*[48] theoretically and numerically investigated the VIV of a cylinder linked to linear and bistable springs. They demonstrated that the spring's bistability initiates the snap-through motion of the cylinder, which expands the range of reduced velocity and increases the cylinder's oscillation amplitude.

Motivated by the prospective energy-harvesting application of piezoelectric materials, various studies on snap-through have been conducted to gain insights into the dynamics and energy-harvesting performance of a flexible sheet.[41,42,44] Betts *et al.*[46] explored the effects of thickness, aspect ratio, and piezoelectric area on the energy performance of a bistable piezoelectric sheet undergoing snap-through oscillations. They found that a higher power output can be obtained by increasing the sheet's thickness while maintaining the bistability to achieve large deformations. The enhancement of energy-harvesting efficiency was further explored by optimizing the systemic parameters.[49,50] Meanwhile, the instability and post-critical behavior of a clamped and buckled sheet were experimentally and numerically studied by Kim *et al.*[41] They explored the effects of mass and length ratio on the sheet's instability and provided some suggestions for refining the generator design. Likewise, Kim *et al.*[43] developed a novel triboelectric nanogenerator based on the bistability of the pre-compressed buckled sheet and investigated its energy-harvesting performance at different wind speeds and wall distances. The findings indicated that the energy extraction efficiency was much greater than that of the flutter-based counterparts, and the cut-in speed and contact pattern of the snapping system were heavily related to the sidewall distance. More recently, Kim *et al.*[42] further conducted an experimental investigation on the dynamic characteristics of two tandem-arranged snapping sheets and pointed out the potential application of snap-through harvester arrays. Although very insightful, the above studies only focus on the compressed sheet with two ends clamped. To our best knowledge, no research has examined the effect of boundary conditions (BCs) on the sheet's energy-harvesting efficiency, especially combined with fatigue durability in snap-through oscillation, which motivates us to bridge this research gap.

In this study, we investigate the effects of different boundary conditions, including clamped ends, pinned ends, clamped–pinned combinations, and torsional elastic end (torsional spring), on the dynamics

and energy-harvesting performance of a snapping sheet in a computational environment. The Reynolds number was selected at Re = 100, considering the snapping sheet's benefit of working at low speeds (Reynolds numbers), and thus inspiring larger oscillation amplitudes, compared to flutter-based energy harvesters.[5,41–43,48] The paper is organized as follows: in Sec. II, the problem description and simulation methods are introduced. The detailed results are presented and discussed in Sec. III. Some appropriate conclusions are drawn in Sec. IV.

II. PROBLEM DESCRIPTION AND METHODOLOGY

This section describes a schematic of the physical problem and the governing equations with its numerical simulation method. We also define the key factors that evaluate the energy-harvesting performance of the snap-through system.

A. Problem description

Figure 1 shows the schematic of the fluid–structure system, with the snapping sheet harvesting energy via snap-through from an incompressible fluid of density ρ_f and kinematic viscosity ν at a uniform velocity U. At the center of the two-dimensional (2D) domain is placed a horizontal, initially compressed sheet with length L, bending stiffness EI, stretching stiffness EA, and line density ρ_s. The sheet is compressed with compression $\Delta L = L - L_0$, and its ends are clamped, pinned, or connected to a linear torsional spring.

In this study, the thin sheet is assumed to be a purely elastic plate exhibiting large deformation but weak electrotechnical coupling behavior. As such, its dynamics are governed by the following geometrical nonlinear structure equations:[51–53]

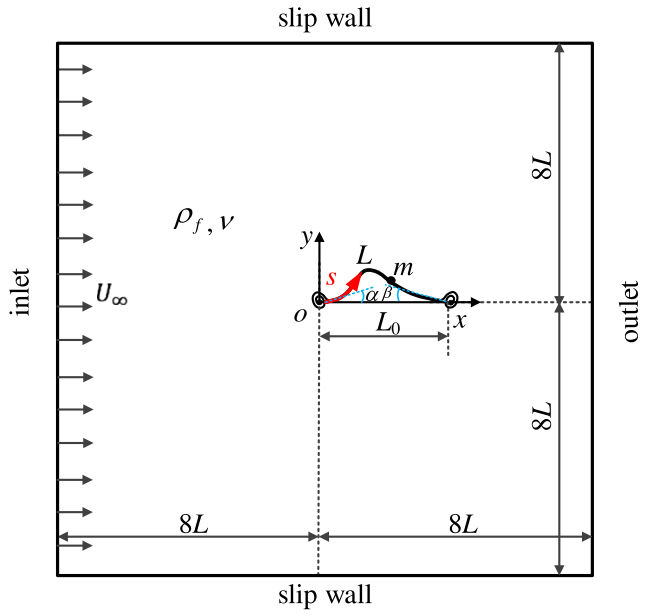

FIG. 1. Schematic of a pre-compressed sheet with length L in a uniform flow. The distance between the front and rear ends is compressed to be L_0, with the ends pinned, clamped, or connected to a linear torsional spring. The front spring locates at the coordinate origin O.

$$\rho_s \frac{\partial^2 \boldsymbol{X}}{\partial t^2} = \frac{\partial}{\partial s}\left[EA\left(1 - \left(\frac{\partial \boldsymbol{X}}{\partial \boldsymbol{s}} \cdot \frac{\partial \boldsymbol{X}}{\partial \boldsymbol{s}}\right)^{-1/2}\right)\frac{\partial \boldsymbol{X}}{\partial \boldsymbol{s}} - \frac{\partial}{\partial \boldsymbol{s}}\left(EI\frac{\partial^2 \boldsymbol{X}}{\partial \boldsymbol{s}^2}\right)\right] + \boldsymbol{F}_f + \boldsymbol{F}_{fs} + \boldsymbol{F}_{rs}, \tag{1}$$

with the boundary conditions

$$X = (0, 0), \quad \frac{\partial \boldsymbol{X}}{\partial \boldsymbol{s}} = (\cos\alpha, \sin\alpha) \tag{2}$$

and

$$X = (L, 0), \quad \frac{\partial \boldsymbol{X}}{\partial \boldsymbol{s}} = (-\cos\beta, \sin\beta), \tag{3}$$

where s is the Lagrangian coordinate along the plate, $\boldsymbol{X}$ is the position vector of the sheet, EI and EA are the structural bending and stretching stiffness, respectively; $\boldsymbol{\rho}_s$ denotes the line density of structure; $\boldsymbol{F}_f$ is the fluid loading exerted on the flexible sheet; $\boldsymbol{F}_{fs}$ and $\boldsymbol{F}_{rs}$ represent the forces resulting from the front and rear rotational springs, which can be obtained by $\boldsymbol{F}_{fs} = k_{fs}\alpha$ and $\boldsymbol{F}_{rs} = k_{rs}\beta$, respectively. α and β are 0 in the springs' natural state in the absence of external disturbances, i.e., the sheet's precompression and fluid forces exerted on the sheet. Upon subjecting the sheet to an initial compression at a specific ratio first, the values of the two deflection angles α and β (as defined in Fig. 1), along with the initial shape of the sheet, are passively determined by the stiffness of rotational spring and the sheet's intrinsic stiffness. Subsequently, as the fluid–structure interaction (FSI) simulation initiates and progresses, both α and β, as well as the sheet's shape, dynamically adapt in response to the instantaneous fluid forces. It should also be mentioned that, under clamped boundary conditions, both α and β consistently remain at 0, even when external disturbances are introduced during the simulation.

The flow dynamics can be described by the incompressible Navier–Stokes equations as follows:

$$\nabla \cdot \boldsymbol{u} = 0, \tag{4}$$

$$\frac{\partial \boldsymbol{u}}{\partial t} + \boldsymbol{u} \cdot \nabla \boldsymbol{u} = -\frac{1}{\rho_f}\nabla \boldsymbol{p} + \nu \nabla^2 \boldsymbol{u} + \boldsymbol{f}_e, \tag{5}$$

where $\boldsymbol{u}$ is the velocity, $\boldsymbol{p}$ is the pressure, $\boldsymbol{\rho_f}$ is the density, ν is the kinematic viscosity, and $\boldsymbol{f}_e$ is the body force term exerted on the flow field from the structure.

The characteristic quantities ρ_f, L, and U_∞ are chosen as repeating variables to parameterize the above energy-harvesting system. As such, Eqs. (1)–(3) can be nondimensionalized as

$$m^* \frac{\partial^2 \boldsymbol{X}^*}{\partial t^{*2}} = \frac{\partial}{\partial \boldsymbol{s}^*}\left[EA^*\left(1 - \left(\frac{\partial \boldsymbol{X}^*}{\partial \boldsymbol{s}^*} \cdot \frac{\partial \boldsymbol{X}^*}{\partial \boldsymbol{s}^*}\right)^{-1/2}\right)\frac{\partial \boldsymbol{X}^*}{\partial \boldsymbol{s}^*} - \frac{\partial}{\partial \boldsymbol{s}^*}\left(EI^*\frac{\partial^2 \boldsymbol{X}^*}{\partial \boldsymbol{s}^{*2}}\right)\right] + \boldsymbol{F}_f^* + \boldsymbol{F}_{fs}^* + \boldsymbol{F}_{rs}^*, \tag{6}$$

$$\nabla^* \cdot \boldsymbol{u}^* = 0, \tag{7}$$

$$\frac{\partial \boldsymbol{u}^*}{\partial t^*} + \boldsymbol{u}^* \cdot \nabla^* \boldsymbol{u}^* = -\nabla^* p^* + \frac{1}{Re}\nabla^{*2}\boldsymbol{u}^* + \boldsymbol{f}_e^*. \tag{8}$$

For ease of discussion, the definitions of the dimensionless parameters in Eqs. (6)–(8) are listed in Table I alphabetically. In this study, the fluid domain has a length of $L_f^* = 16$ and a height of $H_f^* = 16$ to

TABLE I. Definition and chosen values of key dimensionless parameters used in this study.

Dimensionless parameter	Definitions	Baseline values or ranges
Stretching stiffness	$EA^* = EA/\rho_f U^2 L$	1000
Bending stiffness	$EI^* = EI/\rho_f U^2 L^3$	0.001–0.004
External force per unit volume	$\boldsymbol{f}_e^* = \boldsymbol{f}_e L/V_{max}^2$	–[a]
Fluid loading	$\boldsymbol{F}_f^* = \boldsymbol{F}_f/\rho_f U^2$	–
Height of fluid domain	$H_f^* = H_f/L$	16
Curvature	$\kappa^* = \kappa L$	–
Front rotational spring stiffness	$k_{fs}^* = k_{fs}/\rho_f U^2 L^3$	$0–1.5\times10^{-4}$, ∞[b]
Rear rotational spring stiffness	$k_{rs}^* = k_{rs}/\rho_f U^2 L^3$	$0–1.5\times10^{-4}$, ∞
Length of the fluid domain	$L_f^* = L_f/L$	16
Gradient operator	$\nabla^* = L\nabla$	–
Mass ratio	$m^* = \rho_s/\rho_f L$	1.0–4.0
Pressure	$p^* = p/\rho_f U^2$	–
Reynolds number	$Re = UL/\nu$	100
Lagrangian coordinate	$s^* = s/L$	–
Time	$t^* = Ut/L$	–
Velocity	$\boldsymbol{u}^* = \boldsymbol{u}/V_{max}$	–

[a]The symbol "–" indicates that the corresponding parameter is updated in the simulation.
[b]"0" means the simple support at the sheet's end, and "∞" corresponds to the clamped constraint of the sheet's end.

simulate an infinite region. The baseline mechanical properties of the sheet are assumed to be $EI^* = 0.001$ and $m^* = 1.0$, consistent with those in Kim's experimental studies.[41,42] A stretching stiffness $EA^* = 1000$ is adopted to maintain the inextensibility of the sheet (well-supported by Kim's experimental configurations). In consideration of the lower cut-in speed inherent to snapping-based energy harvesters, a fixed Reynolds number (Re) of 100 was employed as a representative low-Re scenario to explore the dynamics and energy-harvesting performance of snapping sheet across various configurations. The front and rear torsional spring stiffnesses k_{fs}^* and k_{rs}^* are set to be 0, $+\infty$, or in the range of $0–1.5\times10^{-4}$ to represent pinned, clamped, and elastically mounted conditions, respectively.

In this study, to investigate the energy-harvesting performance of the sheet, the sheet's mechanical energy is evaluated as follows, excluding the tensional potential energy,

$$E = \frac{\rho_s}{2}\int_0^L \left(\frac{\partial \boldsymbol{X}}{\partial t}\right)^2 ds + \frac{EI}{2}\int_0^L \left(\frac{\partial^2 \boldsymbol{X}}{\partial s^2}\right)^2 ds, \tag{9}$$

where the first term on the right-hand side (R.H.S) of Eq. (9) denotes the sheet's kinetic energy, and the second term is the bending potential energy.

To further analyze the effectiveness of energy harvesting and the contributions of the sheet's different components, the time-averaged mechanical energy and the distributed energy density along the sheet are defined as follows:

$$\bar{E} = \frac{\rho_S}{2T_f}\int_t^{t+T_f}\int_0^L \left(\frac{\partial \boldsymbol{X}}{\partial t}\right)^2 dsdt + \frac{EI}{2T_f}\int_t^{t+T_f}\int_0^L \left(\frac{\partial^2 \boldsymbol{X}}{\partial s^2}\right)^2 dsdt, \tag{10}$$

$$E_{\mathrm{d}} = \frac{\rho_s}{2}(\partial \boldsymbol{X}/\partial t)^2 + \frac{EI}{2}(\partial^2 \boldsymbol{X}/\partial s^2)^2, \tag{11}$$

$$\bar{E}_{\mathrm{d}} = \frac{\rho_S}{2T_f}\int_t^{t+T_f} \left(\frac{\partial \boldsymbol{X}}{\partial t}\right)^2 dt + \frac{EI}{2T_f}\int_t^{t+T_f} \left(\frac{\partial^2 \boldsymbol{X}}{\partial s^2}\right)^2 dt, \tag{12}$$

where T_f is the flapping period of the sheet, and the first and second terms on the R.H.S of Eq. (10) represent the time-averaged kinetic and potential energy coefficients, respectively. On the R.H.S of Eqs. (11) and (12) are the temporal kinetic and potential, time-averaged kinetic and potential energies distributed along the sheet, respectively. For ease of reference, the corresponding dimensionless energy coefficients are elaborated in Table II.

B. Methodology and validation

To facilitate this study, the incompressible two-dimensional nine-discrete-velocity-set multiple-relaxation-time lattice Boltzmann equation (D2Q9 MRT LBE) mode is employed to simulate the fluid dynamics[18,54–58]

$$f_\alpha(x + \boldsymbol{c}_\alpha\Delta t, t + \Delta t) - f_\alpha(x,t) = -\boldsymbol{M}^{-1}\boldsymbol{S}\boldsymbol{M}\left(f_\alpha(x,t) - f_\alpha^{eq}(x,t)\right) - \boldsymbol{M}^{-1}(I - S/2)Mg_\alpha(x,t)\Delta t, \tag{13}$$

where $f_\alpha(x, t)$ is the distribution function for particles having a velocity $\boldsymbol{c}_\alpha$ at the position $\boldsymbol{x}$ and time t, with α indicating its propagation direction. On the R.H.S of this equation, $\boldsymbol{S}$ is the non-negative diagonal relaxation matrix, $\boldsymbol{I}$ is the identity matrix, $\boldsymbol{M}$ denotes the transformation matrix, and f_α^{eq} is the local equilibrium distribution function, which can be defined as

$$f_\alpha^{eq} = w_\alpha\left[\rho_f + \rho_{f0}\left(\frac{\boldsymbol{c}_\alpha\cdot\boldsymbol{u}}{c_s^2} + \frac{(\boldsymbol{c}_\alpha\cdot\boldsymbol{u})^2}{2c_s^4} - \frac{\boldsymbol{u}^2}{2c_s^2}\right)\right], \tag{14}$$

where w_α is the weighting factor, ρ_{f0} is the fluid density, c_s is the speed of sound, and ρ_{f0} is the mean fluid density. The force scheme proposed by Guo *et al.*[57] is imposed to consider the presence of the structure

$$g_\alpha = w_\alpha\left(\frac{\boldsymbol{c}_\alpha - \boldsymbol{u}}{c_s^2} + \frac{\boldsymbol{c}_\alpha\cdot\boldsymbol{u}}{c_s^4}\boldsymbol{c}_\alpha\right)\cdot\boldsymbol{f}_e, \tag{15}$$

where $\boldsymbol{f}_e$ is the external force. The variable velocity $\boldsymbol{u}$ and density ρ_f can be calculated by

$$\rho_f = \sum_\alpha f_\alpha, \quad \boldsymbol{u} = \sum_\alpha \boldsymbol{c}_\alpha f_\alpha + 1/2\boldsymbol{f}_e\Delta t. \tag{16}$$

During the simulation, a uniform velocity U_∞ is set at the upstream boundary realized by the halfway bounce-back scheme,[59] the side boundaries are defined as slip walls also implemented by halfway bounce-back scheme,[59] and a constant pressure boundary is specified at the downstream boundary with the non-equilibrium extrapolation scheme adopted.[54,55,57,60,61]

A geometrical nonlinear co-rotational finite element method (FEM) is used to describe the sheet's dynamics governed by Eq. (1).[28] The structure is discretized into two-node frame elements based on the Bernoulli–Euler beam theory, with each node containing two

TABLE II. Definition of the evaluated dimensionless energetic coefficients.

Dimensionless parameter	Definitions
Instantaneous kinetic energy	$E_k^* = 0.5\rho_s \int_0^L (\partial \boldsymbol{X}/\partial t)^2 ds / \left(0.5\rho_f L^2 U^2\right)$
Instantaneous potential energy	$E_p^* = 0.5EI \int_0^L \left(\partial^2 \boldsymbol{X}/\partial s^2\right)^2 ds / \left(0.5\rho_f L^2 U^2\right)$
Instantaneous total energy	$E^* = E_p^* + E_k^*$
Time-averaged kinetic energy	$\bar{E}_k^* = 0.5\frac{\rho_S}{T_f} \int_t^{t+T_f} \int_0^L (\partial \boldsymbol{X}/\partial t)^2 ds dt / \left(0.5\rho_f L^2 U^2\right)$
Time-averaged potential energy	$\bar{E}_p^* = 0.5\frac{EI}{T_f} \int_t^{t+T_f} \int_0^L \left(\partial^2 \boldsymbol{X}/\partial s^2\right)^2 ds dt / \left(0.5\rho_f L^2 U^2\right)$
Time-averaged total energy	$\bar{E}^* = \bar{E}_p^* + \bar{E}_k^*$
Distributed kinetic energy	$E_{dk}^* = 0.5\rho_s (\partial \boldsymbol{X}/\partial t)^2 / \left(0.5\rho_f L U^2\right)$
Distributed potential energy	$E_{dp}^* = 0.5EI \left(\partial^2 \boldsymbol{X}/\partial s^2\right)^2 / \left(0.5\rho_f L U^2\right)$
Distributed total energy	$E_d^* = E_{dk}^* + E_{dp}^*$
Time-averaged distributed kinetic energy	$\bar{E}_{dk}^* = 0.5\frac{\rho_S}{T_f} \int_t^{t+T_f} (\partial \boldsymbol{X}/\partial t)^2 dt / \left(0.5\rho_f L U^2\right)$
Time-averaged distributed potential energy	$\bar{E}_{dp}^* = 0.5\frac{EI}{T_f} \int_t^{t+T_f} \left(\partial^2 \boldsymbol{X}/\partial s^2\right)^2 dt / \left(0.5\rho_f L U^2\right)$
Time-averaged distributed total energy	$\bar{E}_d^* = \bar{E}_{dk}^* + \bar{E}_{dp}^*$

translational displacements and one rotational angle. The geometrical nonlinearity is handled by using the co-rotational scheme, which has been widely used to solve problems with large-displacement and small-strain.[62–64] In this numerical scheme, a local coordinate system moves with each discrete beam element, by which the structural motion is split into the large rigid motion and small pure deformation of the structure. As such, the problem of large-displacement and small-strain deformation is resolved by coordinate transformation between the co-rotational local and global coordinate systems. Furthermore, the Newmark method is adopted for time discretization. The Newton–Raphson iteration is applied in each time step to reach the structure's dynamic equilibrium, as shown in the following equation:

$$\boldsymbol{K}_{n,i}^{GT} \Delta \boldsymbol{X}_{n,i} = \boldsymbol{F}_n^a - \left(\boldsymbol{F}_n^i + \boldsymbol{M}_{n,i}\ddot{\boldsymbol{X}}_{n,i} + \boldsymbol{C}_{n,i}\dot{\boldsymbol{X}}_{n,i}\right), \tag{17}$$

where $\boldsymbol{K}_{n,i}^{GT}$ is the global effective tangent stiffness matrix at the ith iteration of time step n. The R.H.S of the equation indicates the difference between the applied external force $\boldsymbol{F}_n^a$ and the internal restoring force (the second term on the R.H.S of the equation). Three components, i.e., elastic force $\boldsymbol{F}_n^i$, inertial force $\boldsymbol{M}_{n,i}\ddot{\boldsymbol{X}}_{n,i}$, and damping force $\boldsymbol{C}_{n,i}\dot{\boldsymbol{X}}_{n,i}$ are included. $\Delta \boldsymbol{X}_{n,i}$ is the displacement increment per Newton–Raphson iteration.

The interplay between fluid and structure parts is treated by the direct-forcing immersed boundary method (IBM).[65–69] The Lagrangian interaction force density between the fluid and the structural boundary is evaluated by

$$\boldsymbol{F}_f(\boldsymbol{s}, t) = -2\rho_f \frac{\boldsymbol{U}(\boldsymbol{s}, t) - \boldsymbol{u}(\boldsymbol{s}, t)}{\Delta t}, \tag{18}$$

where $\boldsymbol{U} = \partial \boldsymbol{X}/\partial t$ is the structural velocity and $\boldsymbol{u}$ is the fluid velocity at the position of the plate that can be interpolated by $\boldsymbol{u}(\boldsymbol{s}, t) = \int_\Omega \boldsymbol{u}(\boldsymbol{x}, t)\delta(\boldsymbol{x} - \boldsymbol{X}(\boldsymbol{s}, t))dx$ using the 4-points Dirac delta function δ, which is given as follows:

$$\delta_h(\boldsymbol{x} - \boldsymbol{X}) = \frac{1}{h^2} d_h\left(\frac{x - X}{h}\right) d_h\left(\frac{y - Y}{h}\right), \tag{19}$$

$$d_h(r) = \begin{cases} \frac{1}{8}\left(3 - 2|r| + \sqrt{1 + 4|r| - 4r^2}\right), & 0 \le |r| < 1, \\ \frac{1}{8}\left(5 - 2|r| - \sqrt{-7 + 12|r| - 4r^2}\right), & 1 \le |r| < 2, \\ 0, & |r| \ge 2, \end{cases} \tag{20}$$

where r denotes the distance between Lagrangian points and their nearby Eulerian points.

The Lagrangian force $\boldsymbol{F}_f$ is then spread onto the nearby Eulerian grids, enforcing the no-slip and no-penetration boundary conditions on the plate surface by using the following force spreading formula:

$$\boldsymbol{f}_e(\boldsymbol{x}, t) = -\int_\Gamma \boldsymbol{F}_f(\boldsymbol{s}, t)\delta(\boldsymbol{x} - \boldsymbol{X}(\boldsymbol{s}, t))d\boldsymbol{s}. \tag{21}$$

To assess the capability of the structure solver in dealing with significant geometric nonlinearity, we investigate the equilibrium state of a buckled sheet and compare it with both nonlinear elastica theory and experimental measurements. The sheet's edges are clamped, and the post-buckling configuration is achieved by end-shortening ΔL^*. The deformed shapes at $\Delta L^* = 0.25$ are analyzed and compared to predictions from the nonlinear elastica equation and experimental data, as depicted in Fig. 2(a). The substantial agreement observed between the

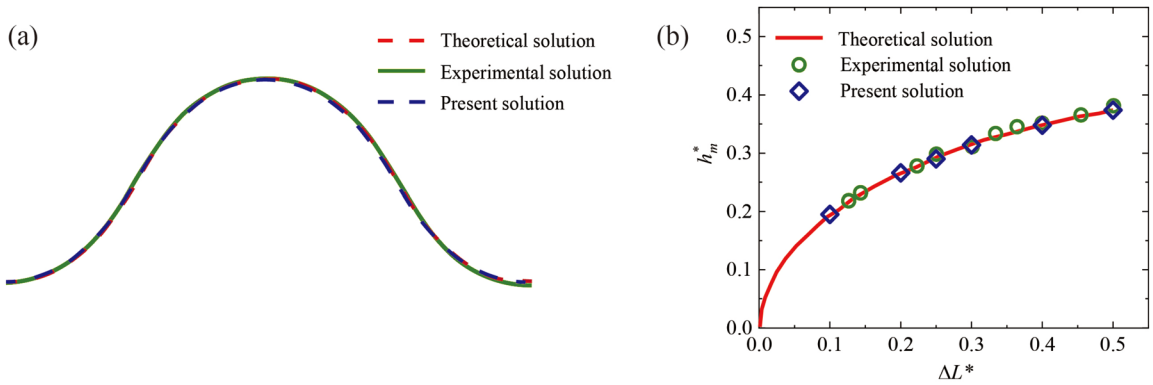

FIG. 2. (a) Initial configurations of the buckled sheet with no external flow for $\Delta L^* = 0.25$. The dashed blue line denotes the present simulation result, and the solid green and dashed red lines represent the theoretical solution obtained from Refs. 41 and 70 and the experimental solution obtained from Ref. 38, respectively. (b) The comparison between the maximum transverse displacement at the middle point h_m^* and ΔL^*.

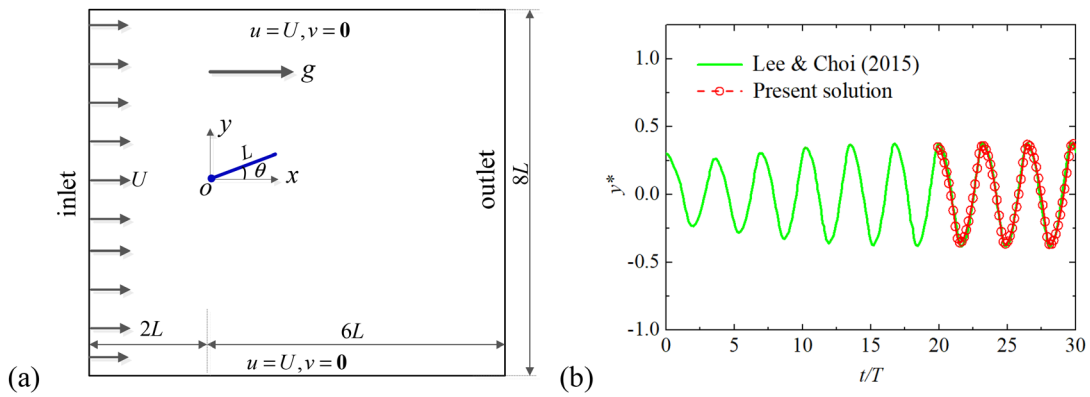

FIG. 3. (a) Schematic of a viscous uniform flow over a flexible plate and (b) time history of the transverse (y-direction) displacement at the plate's trailing edge, where $Re = 200$, $m^* = 1.5$, $EI^* = 0.0015$, $EA^* = 2500$, $F_r = 1.414$.

results validates the accuracy of the proposed model in effectively handling severe geometric nonlinearity. This affirmation is further corroborated by the agreement achieved among the maximum transverse displacements acquired from the theory, experiment, and the numerical solver adopted in the present study, as illustrated in Fig. 2(b).

More details about the current numerical scheme can be found in our previous works,[52,65] and this algorithm is further validated by the case of the viscous fluid flowing over a flexible 2D flag, which has been widely studied in Refs. 67, 71, and 72. The computational configuration is illustrated in Fig. 3(a). The flexible flag is placed in a uniform flow with velocity U and initially held at an angle of 0.1π from the x-axis, with its leading edge pinned and trailing edge free. The gravity is also in the x-direction. The computational domain extends from $(-2L, -4L)$ to $(6L, 4L)$, in which L is the length of the plate. The governing parameters are set the same as those in Ref. 67, with Reynolds number $Re = 200$, mass ratio $m^* = 1.5$, bending stiffness $EI^* = 0.0015$, stretching stiffness $EA^* = 2500$, and Froude number $F_r = 1.414$. Figure 3(b) evaluates the evolution of the transverse displacement (y-direction) of the plate's trailing edge. The good agreement with the previous study ensures the accuracy of the present FSI solver.

C. Convergence study

Three verification cases were performed for the convergence study to ensure the independence of the simulation results on the chosen grid and time step, as listed in Table III, where Δx is the grid spacing, and Δt is the unit time step. In these testing cases, both ends are clamped, and the dimensionless parameters are set as $Re = 100$, $m^* = 1.0$, $EI^* = 0.001$, $EA^* = 1000$, and $\Delta L^* = 0.3$. The differences in the transverse displacement of the sheet's mid-point among the three selected cases are indistinguishable, as shown in Fig. 4. In addition, the time histories of their mechanical energy (E^*) are also in good

TABLE III. Mesh convergence study on energic parameters.

Grid resolution ($\Delta x/L$)	Time step ($U\Delta t/L$)	$\bar{E}_p^*$	$\bar{E}_k^*$	$\bar{E}^*$
1/80	1/8000	0.056	0.030	0.086
1/80	1/4000	0.056	0.030	0.086
1/160	1/8000	0.056	0.031	0.087

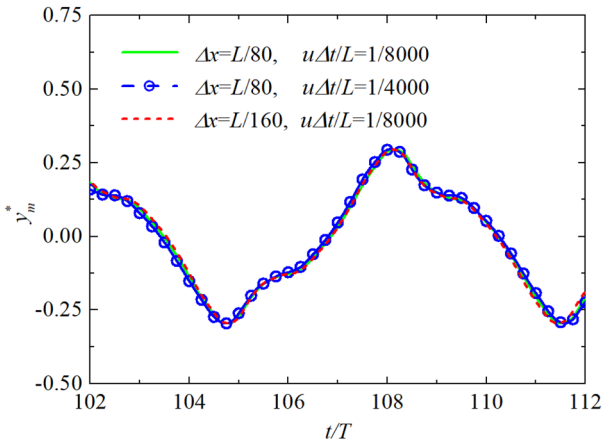

FIG. 4. Instantaneous vertical displacement y_m^* of the sheet's mid-point.

agreement quantitatively. Hence, the setting of $\Delta x = L/80$ and $\Delta t = L/4000u$ is adopted in this study to balance the computational accuracy and efficiency.

To exclude the boundary effect on the computational results, two different computational domains are compared, including $16L \times 16L$ and $24L \times 24L$. The transverse displacement of the sheet's mid-point (y_m^*) and the sheet's mechanical energy (E^*) is compared between two cases, as plotted in Figs. 5(a) and 5(b). The consistent results demonstrate that the simulation domain $16L \times 16L$ is large enough to represent the infinite domain in the current study, and hence the fluid domain of $16L \times 16L$ is used throughout the present study.

III. RESULTS AND DISCUSSION

The primary focus of this study is to systematically examine the effects of the boundary conditions, bending stiffness (EI^*), mass ratio (m^*), and length ratio (ΔL^*) on the energy extraction of the buckled sheet that undergoes snapping motion. The Reynolds number was fixed at 100. A more comprehensive range of parameters was considered, such as the mass ratio m^* ranging from 1.0 to 4.0, the length ratio ΔL^* of the sheet changing from 0.1 to 0.3, and the bending stiffness of the sheet EI^* varying from 0.001 to 0.004. Unless otherwise stated, our simulations will use the following default parameter values: $Re = 100$, $\Delta L^* = 0.1$, $EI^* = 0.001$, $EA^* = 1000$, and $m^* = 1.0$ in the baseline case.

A. Effect of pinned and clamped conditions

Figure 6 gives the sketch of four typical cases to illustrate different BCs on the pre-compressed elastic sheet, where 0 and ∞ indicate pinned and clamped BCs, respectively. For example, the "0-∞" in case 2 is to indicate that the left end of the snapped sheet is pinned and

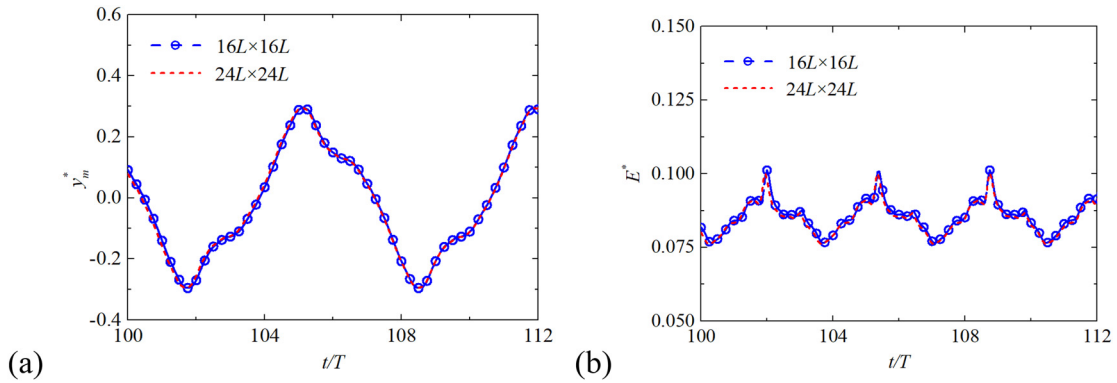

FIG. 5. Comparison of the instantaneous vertical displacement y_m^* (a) and mechanical energy (E^*) (b) between two different computational domains.

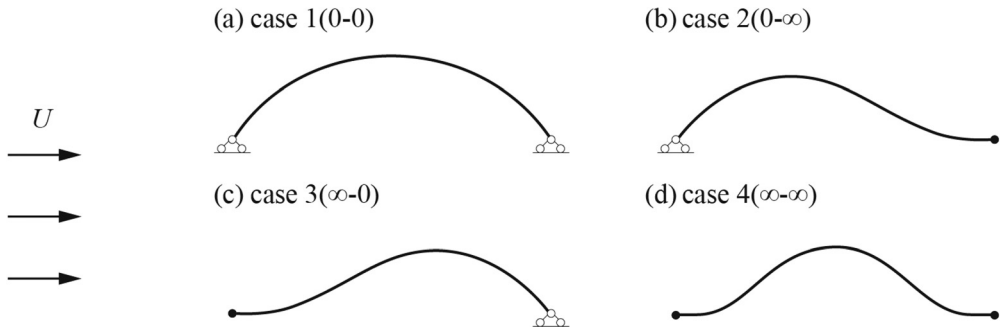

FIG. 6. The sketch of one stable configuration for the flexible sheet in the baseline case, featuring with four different boundary conditions: (a) both ends pinned (case 1: 0-0); (b) left end pinned and right end clamped (case 2: 0-∞); (c) left end clamped and right end pinned (case 3: ∞-0); and (d) both ends clamped (case 4: ∞-∞). In addition, the other stable one for this bistable sheet deflects downward and is symmetrical to the sketch illustrated above.

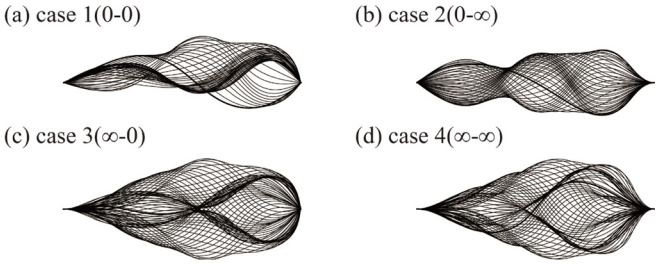

FIG. 7. One-period-enveloping lines of the flexible sheets at four different boundary conditions with (a)–(d) corresponding to the boundary conditions (a)–(d) in Fig. 6.

the right end is clamped. Different BCs are examined to explore the dynamics and energy extraction performance of the flexible sheet at the baseline case, i.e., $Re = 100$, $\Delta L^* = 0.1$, $m^* = 1$, $EA^* = 1000$, and $EI^* = 0.001$. Figure 7 presents the enveloping lines illustrating the sheet's flapping pattern in one oscillation period. Results indicate that the boundary conditions significantly affect the flapping dynamics of the buckled sheet. In particular, an asymmetric vibration mode occurs when both ends are pinned [Fig. 7(a)]; however, when the clamped condition is introduced at any end, the sheet flaps symmetrically [Figs. 7(b)–7(d)]. It is also noted that the left clamped boundary [Figs. 7(c) and 7(d)] produces a larger vibration amplitude as compared with the pinned end [Figs. 7(a) and 7(b)]. The periodic oscillation of the flexible sheet makes it a promising solution for capturing clean energy, including kinetic and potential energies, from the air or water flows.

Figure 8 presents the effects of the four BCs on the time-averaged energy, including potential ($\bar{E}_p^*$), kinetic ($\bar{E}_k^*$), and total ($\bar{E}^*$) energies, in one flapping period. It can be seen that $\bar{E}_p^*$, $\bar{E}_k^*$, and $\bar{E}^*$ all reach peaks at case 2(0-∞), with $\bar{E}_p^*$ and $\bar{E}_k^*$ contributing almost the same portion. However, $\bar{E}_k^*$ (0.018) is almost twice that of the other three cases. This is primarily due to a larger velocity induced in the smaller flapping period in case 2 [see Fig. 8(b)]. Additionally, it is also observed applying clamped support at the sheet's rear end, i.e., in case 2(0-∞) and case 4(∞-∞), significantly benefits potential energy harvesting [see Fig. 8(a)], especially near the rear section of sheet, as indicated in Figs. 9(b) and 9(d). $\bar{E}_p^*$ in case 2 is 0.0209 and case 4 is 0.0201, which is about 23.7% and 18.9% higher than that in case 1 (0.0169). Figures 9(b2) and 9(d2) provide a clear hint for this, demonstrating considerable potential energy generated near the sheet's rear end. In contrast, the front boundary only slightly affects the sheet's energy harvesting on the potential portion, as illustrated by the similar performance of cases 1(0-0) and 3(∞-0) in Fig. 8(a) and Figs. 9(a4) and 9(c4), despite some small variations, i.e., a slight shift in sheet's potential peaks. Meanwhile, the result also indicates that the sheet's rear portion (ranging from $0.5 < s^* < 1.0$) harvests much more energy than the front portion.

To have an insight into the impact of different BCs on the sheet's energy-harvesting performance, we further examine the time–history profiles of total (E^*), potential (E_p^*), and kinetic (E_k^*) energies in one flapping cycle (see Fig. 10) and the instantaneous pressure field, vorticity field, velocity field, force, and velocity distribution along the flexible sheet at selected time instances (see Fig. 11). It can be seen from Fig. 10 that for all cases, the highest potential energy E_p^* and the lowest kinetic energy E_k^* almost occur concurrently and vice versa. In contrast, the appearance of the peak total energy E^* does not follow a single trend, which is nearly consistent with the changes of E_k^* in cases 1–3 while almost synchronizing with that of E_p^* in case 2.

At $t/T_f = 0$ for case 1(0-0) and at $t/T_f = 0.09$ for case 3(∞-0), the minimal E^* is obtained [see the marked hollow circles in Fig. 10(b)]. This is attributed to the relatively small velocity and the smooth curvature along the sheet, as shown in Figs. 11(a1-1) and 11(c1-1). The pressure difference across the sheet [as observed in Figs. 11(a1-1) and 11(c1-1)] in conjunction with the shear layer formed at the peak of sheet's deformation wave [as depicted in Figs. 11(a1-2) and 11(c1-2)] gives rise to the downward, upward, and downward forces acting on the sheet's fore, central, and rear surfaces, respectively, as depicted in Figs. 11(a1-5) and 11(c1-5). These forces induce a reversal of the sheet's deformation wave, causing the sheet to oscillate between Figs. 11(a1-6) to 11(a2-6) and Figs. 11(c1-6) to 11(c2-6). This snapping phenomenon instantaneously releases the potential energy stored in the sheet, particularly in its central and rear sections. Consequently, E_k^* reaches the peak at $t/T_f = 0.183$ for case 1 and at $t/T_f = 0.281$ for case 3 concurrently with the highest E^* [see Figs. 10(b)–10(d)], where the considerable velocity, especially concentrated in the central and rear

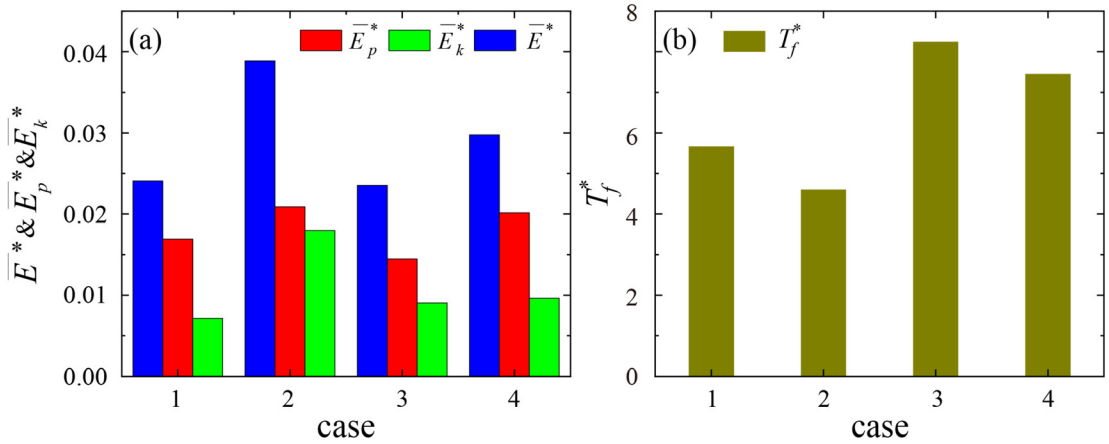

FIG. 8. (a) The time-averaged potential ($\bar{E}_p^*$), kinetic ($\bar{E}_k^*$), and total ($\bar{E}^*$) energies and (b) the flapping period (T_f^*) of the sheet for four typical cases defined in Fig. 6.

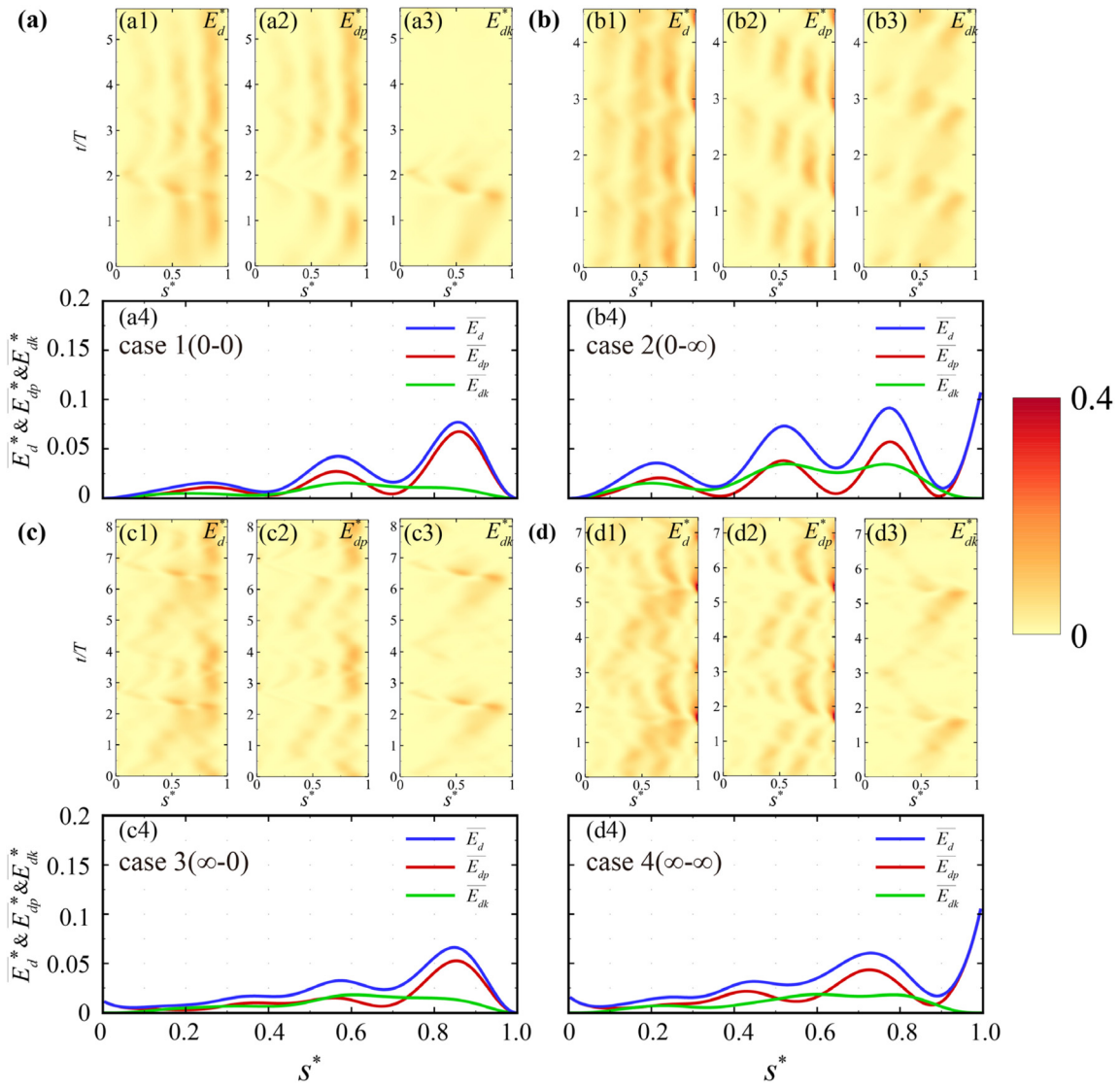

FIG. 9. The instantaneous energy distribution along the flexible sheet, including the total (E_d^*), potential (E_{dp}^*), and kinetic (E_{dk}^*), as illustrated in (1), (2), and (3), respectively, and the time-averaged energy density [shown in Eq. (4)] in one steady snapping period with (a)–(d) corresponding to cases 1–4 in Fig. 6, respectively.

sections of the sheet [see Figs. 11(a2-6) and 11(c2-6)], contributes the peak E_k^* and hence producing a large E^*. Following the snap-through, the fluid force exerted on the sheet propagates the sheet's deformation wave downstream and pushes the sheet downward, especially at the sheet's central part, and hence three deformation peaks form at the sheet at $t/T_f = 0.353$ for case 1 and $t/T_f = 0.418$ for case 3, as indicated in Figs. 11(a3-1) and 11(c3-1). These significant deformations, especially in the sheet's rear part [see Figs. 9(a3) and 9(c3)], generate a considerable E_p^*. In contrast, E_k^* decreases to the minimum at these instants, also evidenced by the minor velocity distribution in Figs. 11(a3-6) and 11(c3-6).

When the sheet's rear end is clamped, a notable improvement in the energy-harvesting performance is obtained in cases 2(0-∞) and 4(∞-∞), compared with the rear-pinned end, as indicated in Fig. 10(b). This is mainly due to the E_p^* and E_k^* increase for case 2 and E_p^* increase for case 4 [see Figs. 10(c) and 10(d)]. In both cases, the sheet's rear part contributes most of E_p^* improvement, as evidenced by the significant curvature shown in Figs. 11(b2) and 11(d1) and considerable energy-harvested promotion near the sheet's back end [see Figs. 9(b) and 9(d)]. At $t/T_f = 0.191$ for case 2 and at $t/T_f = 0.0$ for case 4, the maximum potential energy is stored in the sheet with similar values, as depicted in Fig. 10(c). This outcome is primarily attributed to the rear edge constraint, which leads to pronounced curvature in rear areas. As the snap-through occurs, the stored larger potential energy is swiftly released and converted into kinetic energy, producing a larger velocity distribution, particularly at the sheet's rear part, as demonstrated

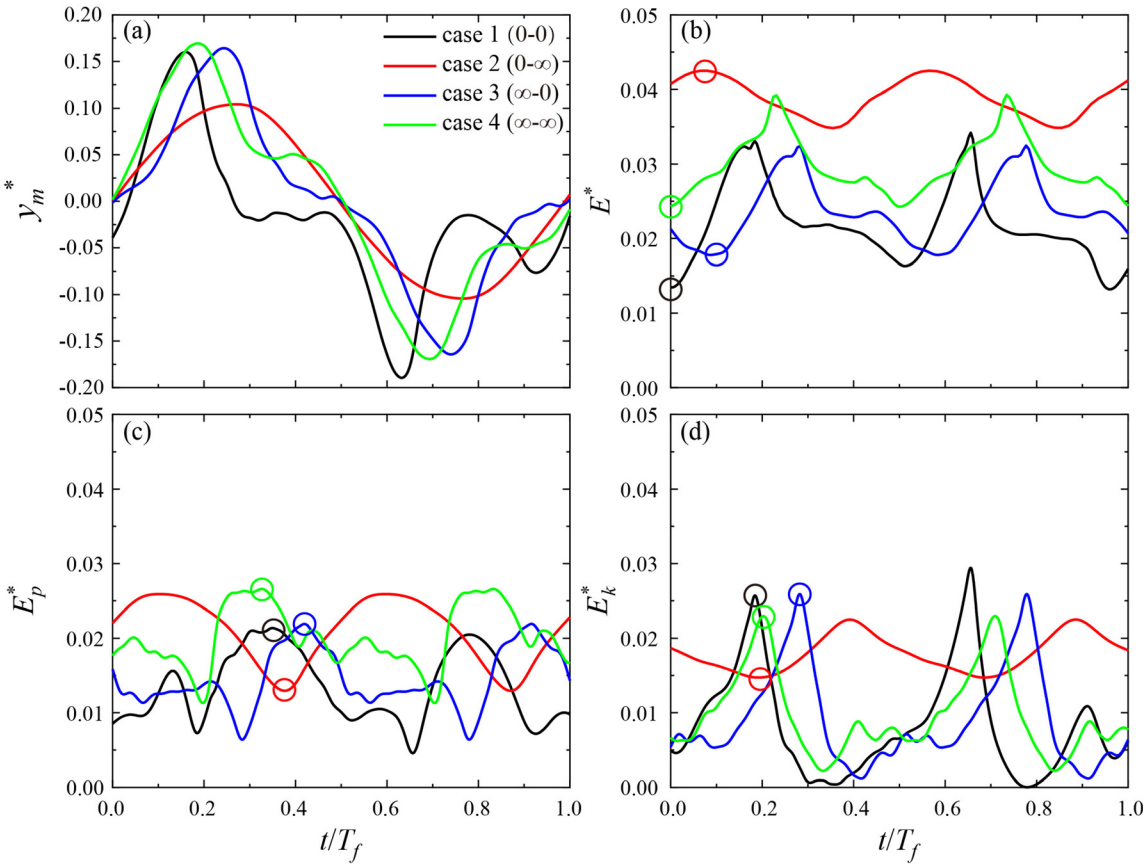

FIG. 10. The time–history of the sheet midpoint transverse displacement y_m^* (a), total E^* (b), potential E_p^* (c), and kinetic E_k^* (d) energies for the four typical cases defined in Fig. 6. The hollow circles indicate the three instances for each case in Fig. 11.

in Figs. 11(b3-6) and 11(d2-6). However, in comparison to case 4 (∞-∞), it is worth noting that the fore-pinned BC in case 2(0-∞) releases the rotation constrain, inducing a substantially larger velocity distributed at the front and central sections of the sheet, as clearly demonstrated by the comparison between Figs. 11(b3-6) and 11(d2-6). As a consequence, the (0-∞) BC outperforms the (∞-∞) BC in terms of energy harvesting [see Fig. 10(b)]. The E_k^* enhancement in case 2 can also be explained from a faster back-and-forth flapping of the sheet, as shown in Fig. 8(b). By evidently improving both E_p^* and E_k^*, case 2(0-∞) becomes the optimal choice for harvesting the sheet's energy with the current configuration.

B. Effect of length ratio

As indicated by Kim *et al.*,[41] the dynamics of the two-end clamped sheet are considerably affected by the sheet's pre-compression. Therefore, in this section, we further explore the ΔL^* effect on the energy extraction performance under different BCs, as shown in Fig. 12. Results indicate that all $\bar{E}_p^*$, $\bar{E}_k^*$, and $\bar{E}^*$ steadily increase as the length ratio ΔL^* increases from 0.1 to 0.3; meanwhile, the potential energy $\bar{E}_p^*$ contributes more to the total energy $\bar{E}^*$ in all cases. For example, $\bar{E}_p^*$ contributes 68.1% to the increase in $\bar{E}^*$ from 0.0388 ($\Delta L^* = 0.1$) to 0.0855 ($\Delta L^* = 0.3$) in case 2 [see Fig. 12(b)]. Larger $\bar{E}_p^*$, $\bar{E}_k^*$, and $\bar{E}^*$ in cases 2(0-∞) and 4(∞-∞) are observed compared to cases 1(0-0) and 3(∞-0), especially in the scenario with larger ΔL^*, i.e., $\Delta L^* = 0.2$ and 0.3. This further indicates that the rear-clamped end outperforms the rear-pinned one on the energy-harvesting performance. For the cases with a rear-clamped end, as shown in Figs. 12(b) and 12(d), the front BC, i.e., front-end pinned in case 2(0-∞) and clamped in case 4(∞-∞), seems to have relatively minimal impact on energy harvesting, especially in the scenario with large length ratios, i.e., $\Delta L^* = 0.3$.

To investigate the dynamics of the sheet, as well as its deformation wave propagation, we examine the flow characteristics in the selected typical case 2 (0-∞) at $\Delta L^* = 0.3$, $EI^* = 0.001$, and $m^* = 1$, as illustrated in Figs. 13 and 14. Two distinct sheet motions are observed, including the streamwise shift [Fig. 13(a3)] and the up–down snap-through [Figs. 13(a1) and 13(a2)]. Initially, at T_1 ($t/T_f = 0.021$), an "S" shape is formed due to the snapping motion [see Fig. 13(a1)]. The shear layers developed at the sheet's lower peak [see Fig. 14(a2)], in combination with the pressure difference at the sheet's rear part [as indicated in Fig. 14(a1)], initiates an upward stroke at the sheet's rear part, as illustrated in Fig. 14(a6). Subsequently, a snapping motion ensues as the sheet undergoes a sudden transformation into a

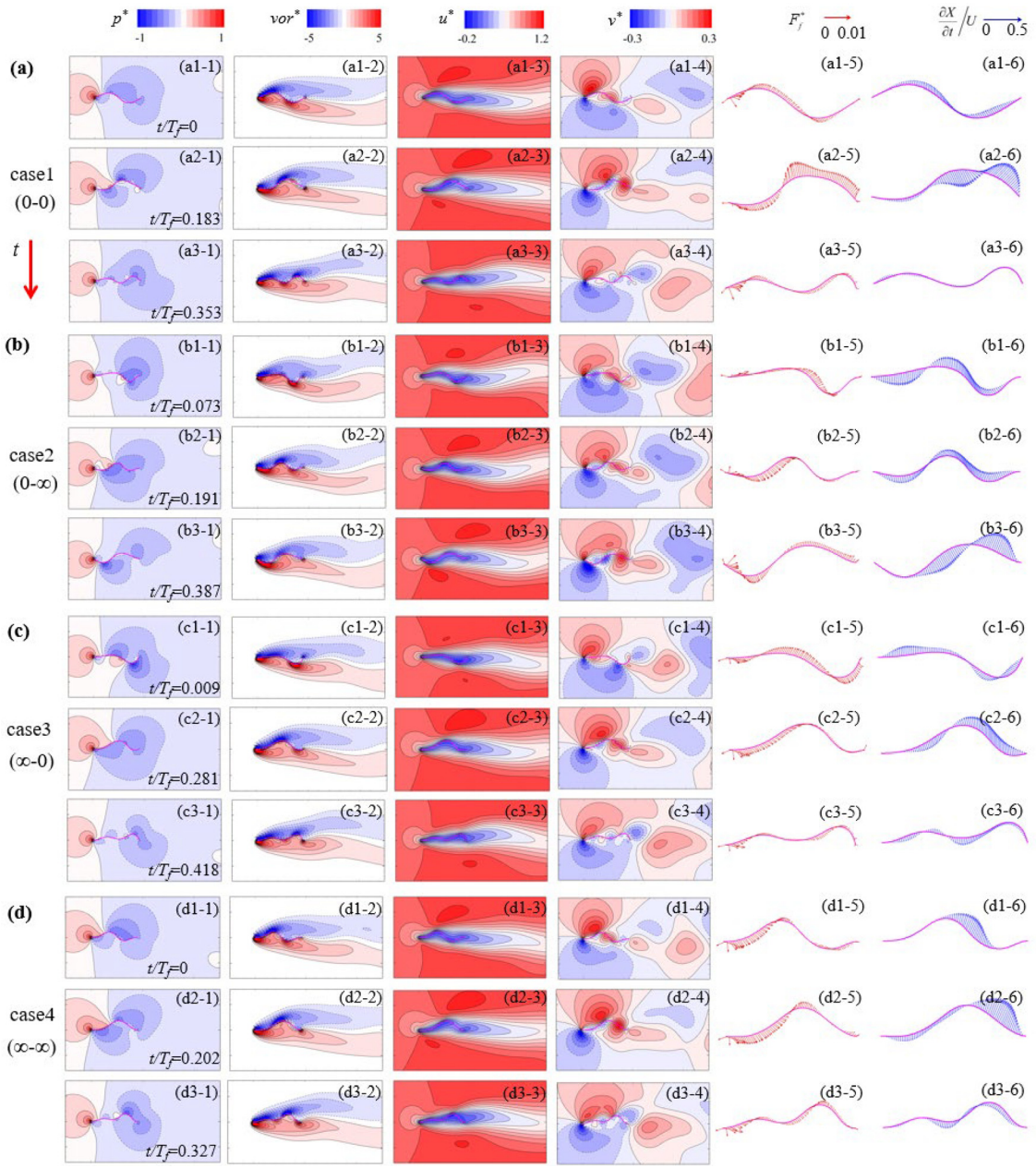

FIG. 11. The instantaneous pressure field, vorticity field, velocity field around the sheet, force, and velocity distribution along the flexible sheet at special time-sequences: (a) case 1(0-0); (b) case 2(0-∞); (c) case 3(∞-0); and (d) case 4(∞-∞). The three instances in this figure correspond to the marked hollow circles in Fig. 10.

symmetrical shape, as depicted in Figs. 13(a2) and 14(b). This transition is accompanied by a notable conversion of potential energy into kinetic energy, culminating in the potential energy reaching its minimum value. Simultaneously, the kinetic energy attains its maximum value, primarily attributed to the substantial velocity present at the sheet's rear section, as clearly illustrated in Figs. 14(b4) and 14(b6). At the symmetrical instant $t/T_f = 0.177$, the windward area induces a higher positive pressure on the upper surface of the sheet's fore part, while the shear layer beneath the sheet's rear edge induces a negative pressure field, as shown in Figs. 14(b1) and 14(b2). The resulting force, as shown in Fig. 14(b5), induces a streamwise shift in the sheet's deformation wave, as observed in Fig. 13(a3). As the sheet's deformation wave propagates streamwise, a pronounced curvature becomes evident near the sheet's rear edge, owing to the constraint imposed by the clamped boundary condition. This results in the potential energy reaching its peak value at $t/T_f = 0.314$. Subsequently, the sheet

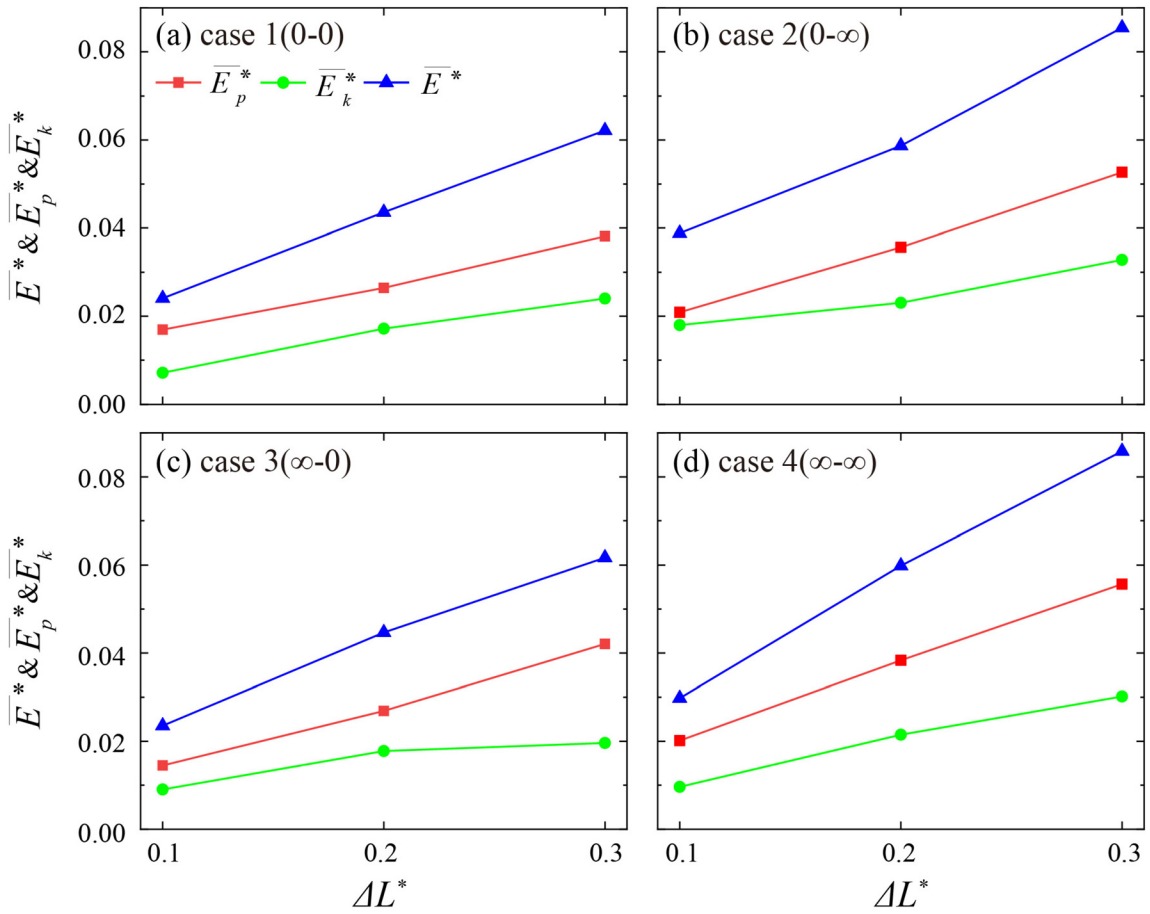

FIG. 12. The time-averaged potential ($\bar{E}^*_p$), kinetic ($\bar{E}^*_k$), and total ($\bar{E}^*$) energies in a stable flapping period under different length ratios and connection ends: (a) case 1(0-0); (b) case 2(0-∞); (c) case 3(∞-0); and (d) case 4(∞-∞).

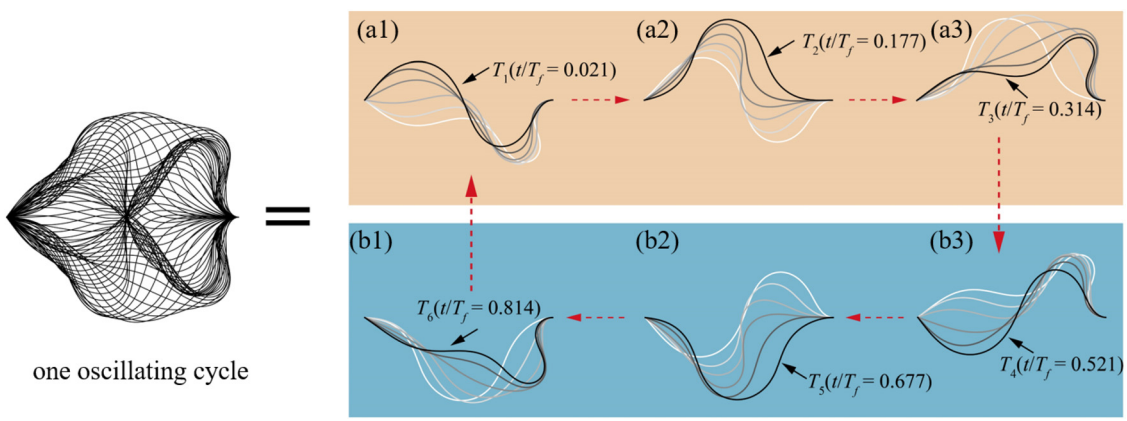

FIG. 13. Superimposed sequential profiles of the sheet in one oscillating cycle to illustrate the deformation wave propagation of the sheet in case 2(0-∞) at $\Delta L^* = 0.3$, $EI^* = 0.001$, and $m^* = 1$. Left is the enveloping lines of the sheet in one snapping cycle. Right is the decomposed sheet motion to highlight the process of wave propagation. In each subgraph, the sheet progresses, starting from the position of light color to that of dark color. The time instances T_1, T_2, and T_3 correspond to the moments with the minimum total energy, maximum kinetic energy, and maximum potential energy, respectively. These time points are defined relative to the moment when the sheet's midpoint crosses the midline.

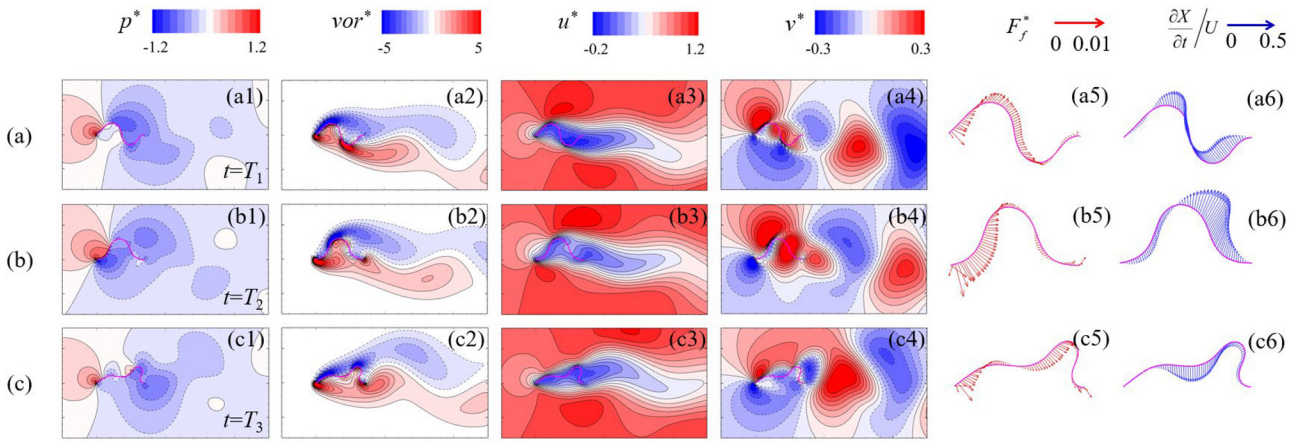

FIG. 14. The instantaneous pressure field, vorticity field, velocity field around the sheet, force, and velocity distribution along the flexible sheet at some typical instances in case 2: 0-∞ at $\Delta L^* = 0.3$, $EI^* = 0.001$, and $m^* = 1$. The three instances in this figure correspond to the marked $t = T_1$, T_2, and T_3 in Fig. 13.

undergoes a downward snap, initiating a similar snapping dynamic as previously described.

To further reveal the contributions of the sheet's various portions on energy harvesting, Fig. 15 plots the time-averaged energy density along the sheet at $\Delta L^* = 0.3$, $EI^* = 0.001$, and $m^* = 1$. $\bar{E}^*_{dp}$ contributes significantly to the overall $\bar{E}^*_d$, with the majority of the contribution coming from the sheet's rear section. This pattern resembles the one at $\Delta L^* = 0.1$ in Fig. 9 but with a considerably greater value due to the larger pre-compression ratio ΔL^*. Figure 16 shows evidence that the rear-clamped BC with $\Delta L^* = 0.3$ has a greater improvement in energy harvesting than the counterpart in Fig. 10 with $\Delta L^* = 0.1$. More precisely, the rear-clamped end enhances the harvesting efficiency on a larger scale by promoting both E^*_p and E^*_k, as illustrated in Figs. 16(c) and 16(d). For instance, the peaks of E^*_p and E^*_k in case 2 increase by about 152.2% and 82.2% due to a higher pre-compression ratio. As to the dynamics of the snapping system, compared to $\Delta L^* = 0.1$ in Fig. 11, a larger pressure difference ($\Delta L^* = 0.3$) can be seen between the top and bottom surfaces of the sheet, as denoted in Fig. 17. It induces a more substantial deformation of the sheet [see the large flapping amplitude in Fig. 16(a)] and increases the snapping velocity along the sheet under the larger $\Delta L^* = 0.3$, hence considerably improving the energy-harvesting efficiency. In addition, Fig. 16(b) illustrates the low influence of front BCs on energy extraction with the sheet in a snapping state at $\Delta L^* = 0.3$. This observation is aligned with the noted similarity in flow dynamics between case 1(0-0) and case 3(∞-0), as well as case 2(0-∞) and case 4(∞-∞), as depicted in Fig. 17. In contrast, the rear BC exerts a remarkable influence on the sheet's deformation and significantly alters the flow dynamics, particularly in the region of streamwise shift, as demonstrated through the comparison between Figs. 17(c) and 17(d).

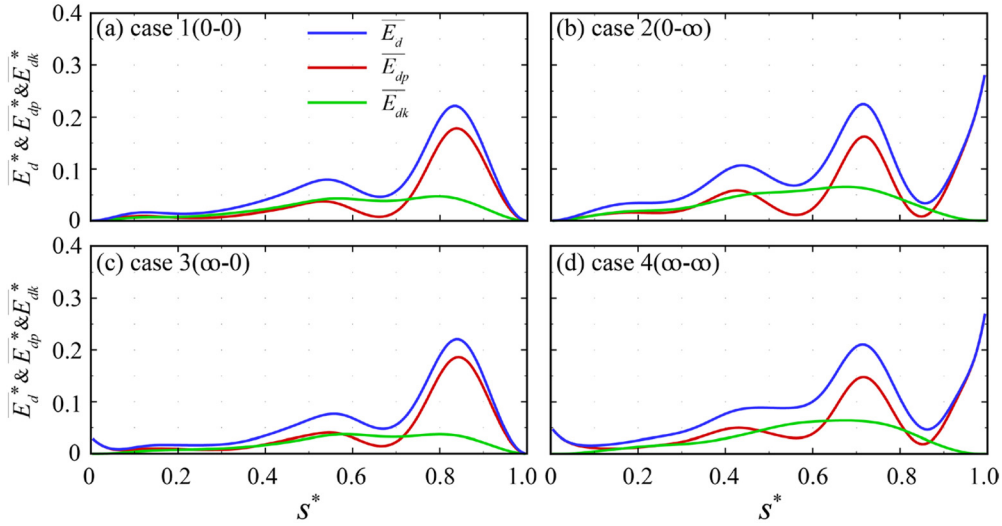

FIG. 15. The time-averaged energy density profile along the sheet for $\bar{E}^*_d$, $\bar{E}^*_{dp}$, and $\bar{E}^*_{dk}$ during a flapping circle: (a) case 1(0-0); (b) case 2(0-∞); (c) case 3(∞-0); and (d) case 4(∞-∞) at $\Delta L^* = 0.3$, $EI^* = 0.001$, and $m^* = 1$.

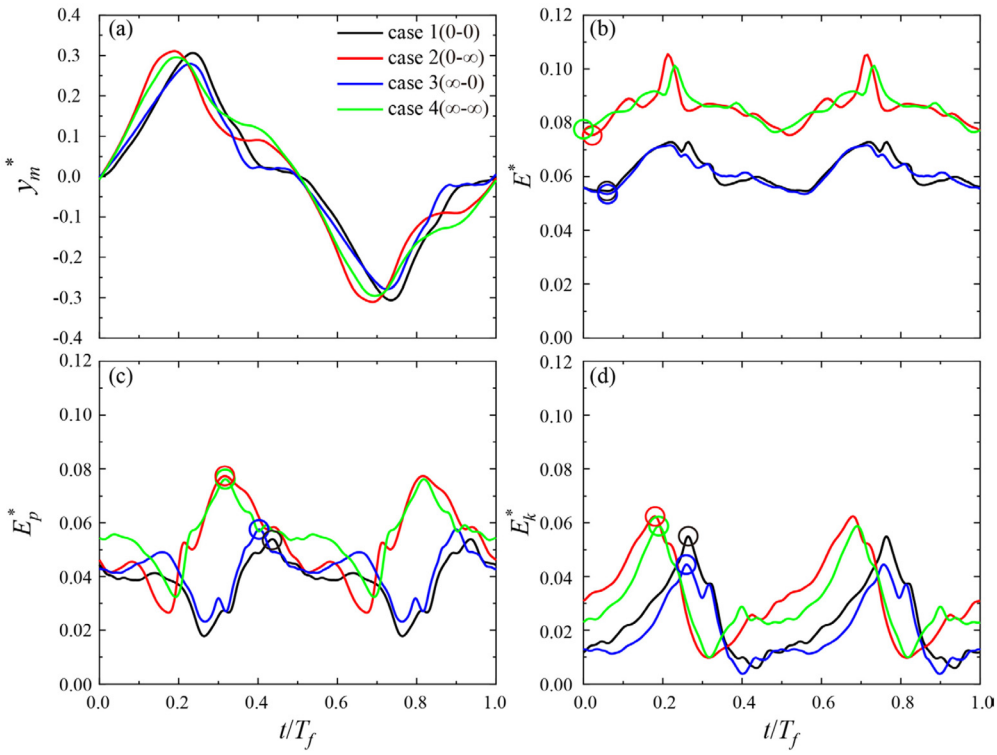

FIG. 16. The time–history of the sheet midpoint transverse displacement y_m^* (a), total E^* (b), potential E_p^* (c), and kinetic E_k^* (d) energies for the four typical cases, defined in Fig. 6, at $\Delta L^* = 0.3$, $EI^* = 0.001$, and $m^* = 1$.

C. Effect of bending stiffness and mass ratio

In addition to the length ratio, the bending stiffness EI^* and mass ratio m^* are also highly connected to the sheet's dynamics and energy extraction capability. Hence, their effects on energy extraction are explored at an efficient length ratio of $\Delta L^* = 0.3$ with four different BCs, as shown in Fig. 18. When the sheet's front edge is pinned, i.e., cases 1(0-0) and 2(0-∞), all $\bar{E}^*$ increase monotonically with m^* and EI^*, with its major contribution to this trend coming from the kinetic energy $\bar{E}_k^*$, as displayed in Figs. 18(b1) and 18(b2) and Figs. 18(c1) and 18(c2). In contrast, $\bar{E}_p^*$ in all case is mainly affected by EI^* and experience a positive correlation with EI^* [see Figs. 18(a1)–18(a4)]. As for $\bar{E}_k^*$, when the sheet has a clamped front-end, i.e., in cases 3(∞-0) and 4(∞-∞), a completely distinct pattern is observed, including periodic flapping (PF) and static deflection (SD) states, as illustrated in Figs. 18(b3) and 18(b4). More specifically, compared to the monotonical increase in $\bar{E}_k^*$ with EI^* and m^* in cases 1 and 2, the similar observation is only valid when $EI^* \leq 0.002$ [see Figs. 18(b1)–18(b4)], and hence both cases achieve optimal performance near $EI^* = 0.002$ and $m^* = 4$, with $\bar{E}_p^* = 0.076$, $\bar{E}_k^* = 0.039$, $\bar{E}^* = 0.115$ for case 3 and $\bar{E}_p^* = 0.099$, $\bar{E}_k^* = 0.098$, $\bar{E}^* = 0.197$ for case 4. This is mainly because the sheet transits into a static deflecting state when $EI^* \geq 0.003$ [see the blue squares in Fig. 18(b)] and thus $\bar{E}_k^*$ drops to near zero, similar to that observed in our previous work.[5]

Figure 19 presents the enveloping lines with $\Delta L^* = 0.3$, $EI^* = 0.004$, and $m^* = 4$ with different BCs. The result shows that a periodic oscillation is observed in cases 1(0-0) and 2(0-∞); in contrast, the sheet keeps almost static in cases 3(∞-0) and 4(∞-∞). It suggests that a front-pinned end can more easily trigger the instability of the snapping sheet, whereas a front-clamped end stabilizes the system.

D. Effect of torsional spring's stiffness at edge

The previous discussion on the sheet's dynamics and energy extraction efficiency is based on ideal BCs, i.e., pinned, clamped, or their combinations. Despite the energy-harvesting effectiveness in one cycle, the sheet's safe durability, also known as fatigue life, which is closely connected to stress fluctuation, is another crucial concern in the periodic snapping situation. The relation between the stress and fatigue life can be characterized by the Basquin equation $\lg\sigma_R = a + b\lg N$, where a and b are two constants, with b always being negative, N stands for the fatigue cycle of the structure, σ_R is the stress amplitude at the fatigue stress ratio R (defined as the ratio of the minimum to highest fatigue stresses, and in this instance, $R = -1$ since the sheet flaps symmetrically).[73–77] It demonstrates that the stress increase directly reduces the sheet's fatigue limits. However, given the ideal boundary conditions, the stress concentration, particularly at the sheet's rear end of the high-energy-efficiency cases (0-∞ and ∞-∞), dramatically increases the stress-fluctuating amplitude at the clamped ends. This greatly degrades the sheet's structural durability and operation safety.[78] To alleviate the stress concentration and hence prolong the sheet's safe durability, the elastically mounted end, which connects the end to a torsional spring, is introduced and contrasted with the clamped one.

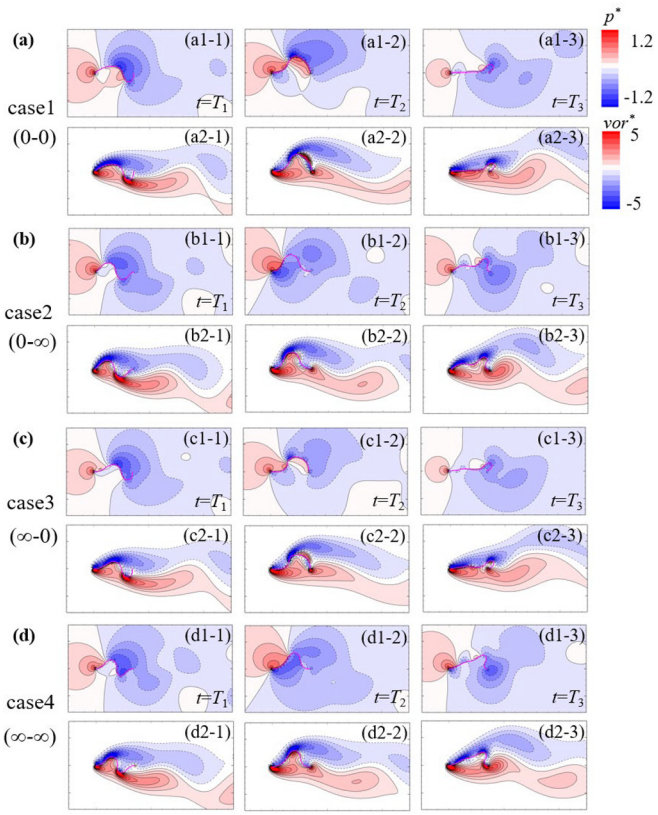

FIG. 17. The instantaneous pressure and vorticity fields at some typical instances in case 1: 0-0 (a), case 2: 0-∞ (b), case 3: ∞-0 (c), case 4: ∞-∞ (d) at $\Delta L^* = 0.3$, $EI^* = 0.001$, and $m^* = 1$. The three instances in this figure correspond to the marked hollow circles in Fig. 16.

The effect of boundary elasticity on the sheet's ability to capture energy is first investigated by varying its flexibility in a certain range, i.e., k_{fs}^* and k_{rs}^* change from 0 to 1.5×10^{-4}, at $EI^* = 0.001$ or 0.004 and $m^* = 1.0$ or 4.0 within the chosen parameter ranges of Sec. II C, as shown in Fig. 20. The outcome indicates in the case of $EI^* = 0.001$ and $m^* = 1.0$, a consistent snap-through pattern, i.e., PF mode, is obtained for the entire spring-stiffness range, as indicated by the red circles in Fig. 20(a2). As for the effect of boundary flexibility, the front-edge spring k_{fs}^* seems to have a negligible impact on $\bar{E}_p^*$, $\bar{E}_k^*$, and $\bar{E}^*$ [which is more clear in Fig. 20(b) for $m^* = 4.0$], whereas $\bar{E}_p^*$, $\bar{E}_k^*$, and $\bar{E}^*$ increase with k_{rs}^*, especially in the range from 0 to 7.5×10^{-5} [see Fig. 21(a), where a pinned front edge ($k_{fs}^* = 0$) is adopted for both initiating snapping easily and maintaining energy harvesting efficiently (refer to Fig. 10)]. This superiority is maintained almost constant as k_{rs}^* continues to increase, as displayed in Fig. 21(a). It indicates that keeping the rear-spring stiffness not less than 7.5×10^{-5} helps enhance the energy extraction at $EI^* = 0.001$ and $m^* = 1.0$. When the mass ratio m^* increases to 4.0, the flapping mode is unaffected, but other energy components, particularly $\bar{E}_k^*$, are clearly enhanced, leading to a significant rise in the overall $\bar{E}^*$, as contrasted between (a) and (b) in both Figs. 20 and 21. The increase in $\bar{E}_k^*$ at $EI^* = 0.001$ and $m^* = 4.0$, which is about 174.6%, is achieved when $k_{fs}^* = 0$ and $k_{rs}^* = 3.75 \times 10^{-5}$.

When the sheet's EI^* increases to 0.004, an utterly distinct pattern on energy contours is observed in Figs. 20(c) and 20(d). Specifically, a narrow region with high energy $\bar{E}^*$ exists in the left-bottom region (PF region). With k_{fs}^* and k_{rs}^* increasing, the sheet transits from a periodic flapping mode to a steady deflected one, and thus $\bar{E}^*$ drops dramatically as a result of lowering of $\bar{E}_k^*$. The sheet's stability seems to be more sensitive to the front end, and the sheet fully develops into SD mode with k_{rs}^* exceeding 7.5×10^{-5} regardless of the k_{fs}^* value [see Figs. 20(c2) and 20(d2)]. This finding indicates that, for a relatively stiffer sheet ($EI^* = 0.004$), retaining the front spring sufficiently flexible improves the sheet's ability to capture energy by activating its periodic flapping mode, as illustrated in Figs. 21(c) and 21(d). This is in line with the early discovery that the front-pinned end might more readily cause the sheet's instability. Figure 21 further shows that when $k_{rs}^* \geq 1.125 \times 10^{-4}$, $\bar{E}^*$ stays nearly constant, making it possible to reduce stress concentration and yet capture energy efficiently by choosing a limited k_{rs}^*. Moreover, the similarity of state distributions of Figs. 20(c2) and 20(d2) indicates that the m^* effect on sheet's instability is not significant, which is consistent with the observation by Kim *et al.*[42]

The time-averaged energy densities at different spring flexibilities are evaluated in two selected cases ($\Delta L^* = 0.3$, $m^* = 1$, $EI^* = 0.001$, and $\Delta L^* = 0.3$, $m^* = 4$, $EI^* = 0.004$) to investigate the spring's stiffness on the energy distribution, as illustrated in Fig. 22. It is clearly observed that the energy distribution features of $\bar{E}_d^*$ and $\bar{E}_{dp}^*$, i.e., the maximum position, are comparable, mainly because a majority of the total energy originates from the potential energy, especially when $m^* = 1$ and $EI^* = 0.001$. Meanwhile, the front boundary barely affects the energy harvested, which can be validated by comparing case I with case III and comparing case II with case IV in Fig. 22(a). However, the gathered energy $\bar{E}_d^*$ appears to stem primarily from the sheet's rear portion, according to Fig. 22(a). This is also valid for the scenario where $m^* = 4$, $EI^* = 0.004$ with $k_{fs}^* = 1.125 \times 10^{-4}$; in this situation, zero $\bar{E}_{dk}^*$ makes $\bar{E}_d^*$ and $\bar{E}_{dp}^*$ equivalent with the sheet evolved into the steady deflection state [see cases III and IV in Fig. 22(b)]. When $k_{fs}^* = 0$, the initiated snapping oscillation triggers a relatively large kinetic energy $\bar{E}_{dk}^*$ along the heavier sheet and thus produces a higher total energy extraction $\bar{E}_d^*$, as indicated by cases I and II of Fig. 22(b). Additionally, the center portion of the sheet is where much of the kinetic energy is distributed, making it the best part for energy harvesting [see Fig. 22(b2)].

As mentioned above, the sheet's fatigue life is one concern in the efficient snapping mode. To further study the sheet's safe durability under different elastic ends, the oscillating amplitude of curvature, which represents the strain-fluctuation amplitude under bending, is extracted along the sheet on two selected cases ($\Delta L^* = 0.3$, $m^* = 1$, $EI^* = 0.001$, and $\Delta L^* = 0.3$, $m^* = 4$, $EI^* = 0.004$) to disclose the relief of stress concentration at edges. Considering the rear stiffness $k_{rs}^* = 1.125 \times 10^{-4}$ is large enough for maintaining energy-harvesting efficiency and the front spring has very little impact on energy extraction of snapping sheet, we adopt the baseline case having $k_{fs}^* = 0$ and $k_{rs}^* = 1.125 \times 10^{-4}$ and compared its performance with the case of $k_{fs}^* = 0$ and $k_{rs}^* = \infty$, as depicted in Fig. 23. In both chosen cases, the rear BCs slightly affect the energy harvested, i.e., 12.8% reduction in

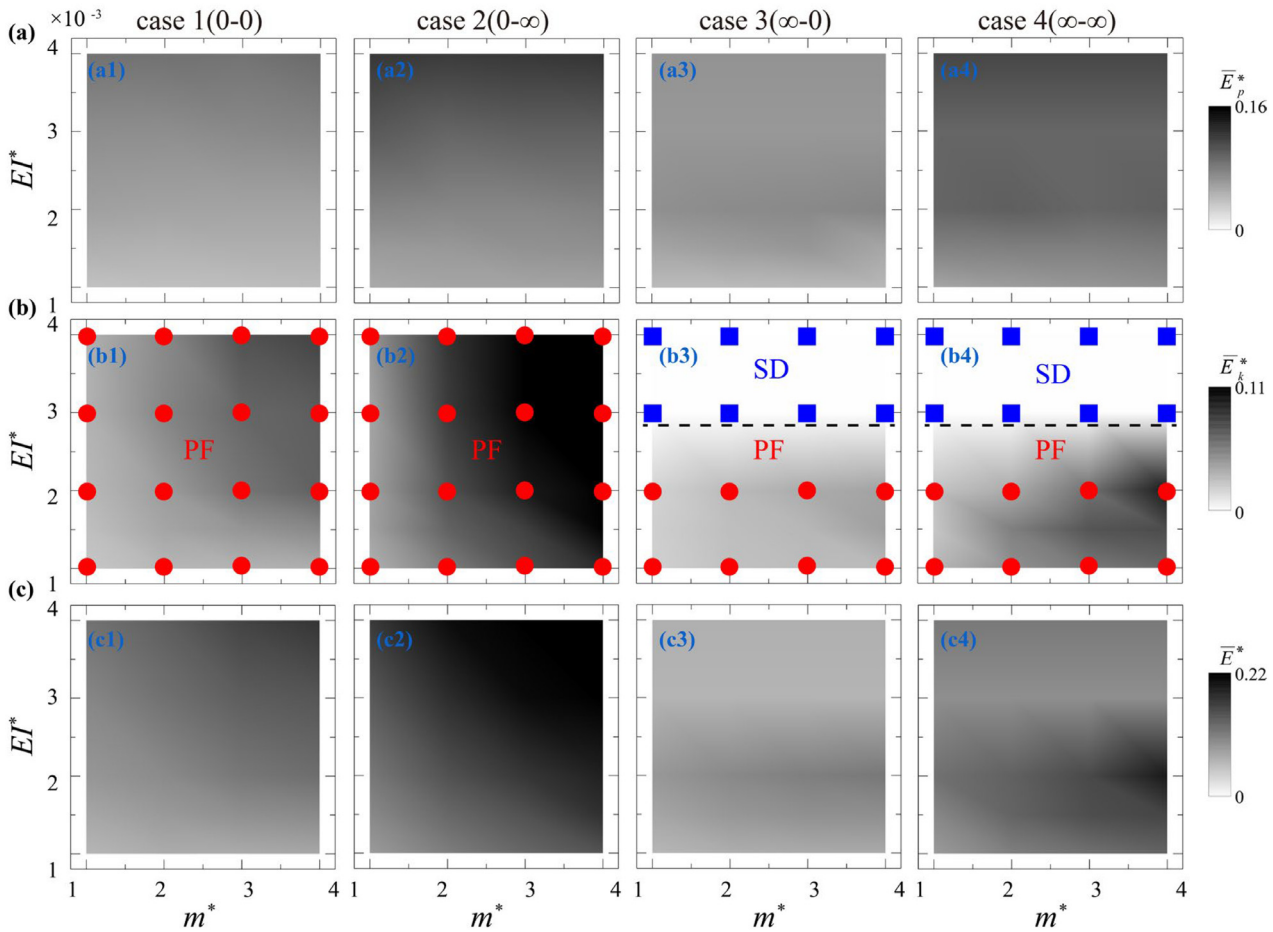

FIG. 18. Contour of the time-averaged potential $\bar{E}_p^*$ (a1)–(a4), kinetic $\bar{E}_k^*$ (b1)–(b4), and total $\bar{E}^*$(c1)–(c4) energies in the map of the bending stiffness EI^* vs mass ratio m^* at different BCs with $\Delta L^* = 0.3$, where the red circulars and blue squares in (b) represent the periodic flapping (PF) and static deflection (SD) states, respectively.

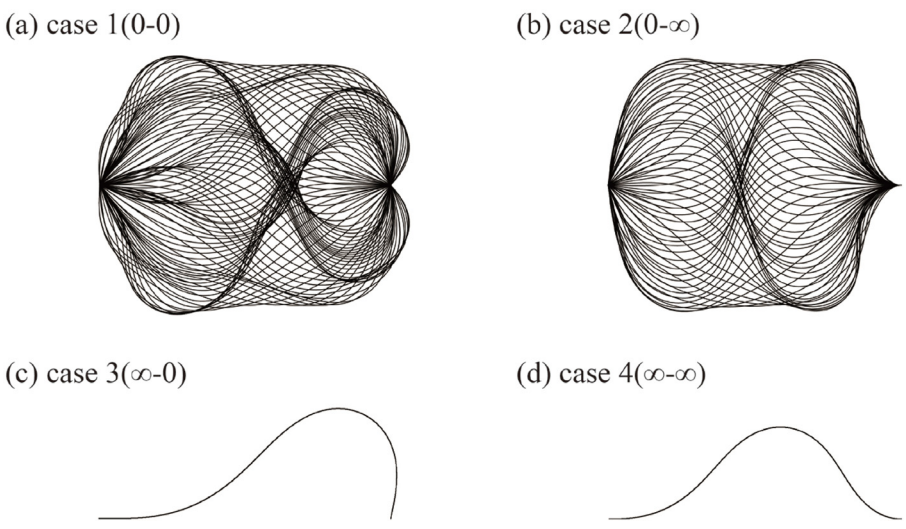

FIG. 19. Enveloping lines of the flexible sheet at $\Delta L^* = 0.3$, $EI^* = 0.004$, and $m^* = 4$ in one flapping period of (a) case 1(0-0); (b) case 2(0-∞); (c) case 3(∞-0); and (d) case 4(∞-∞).

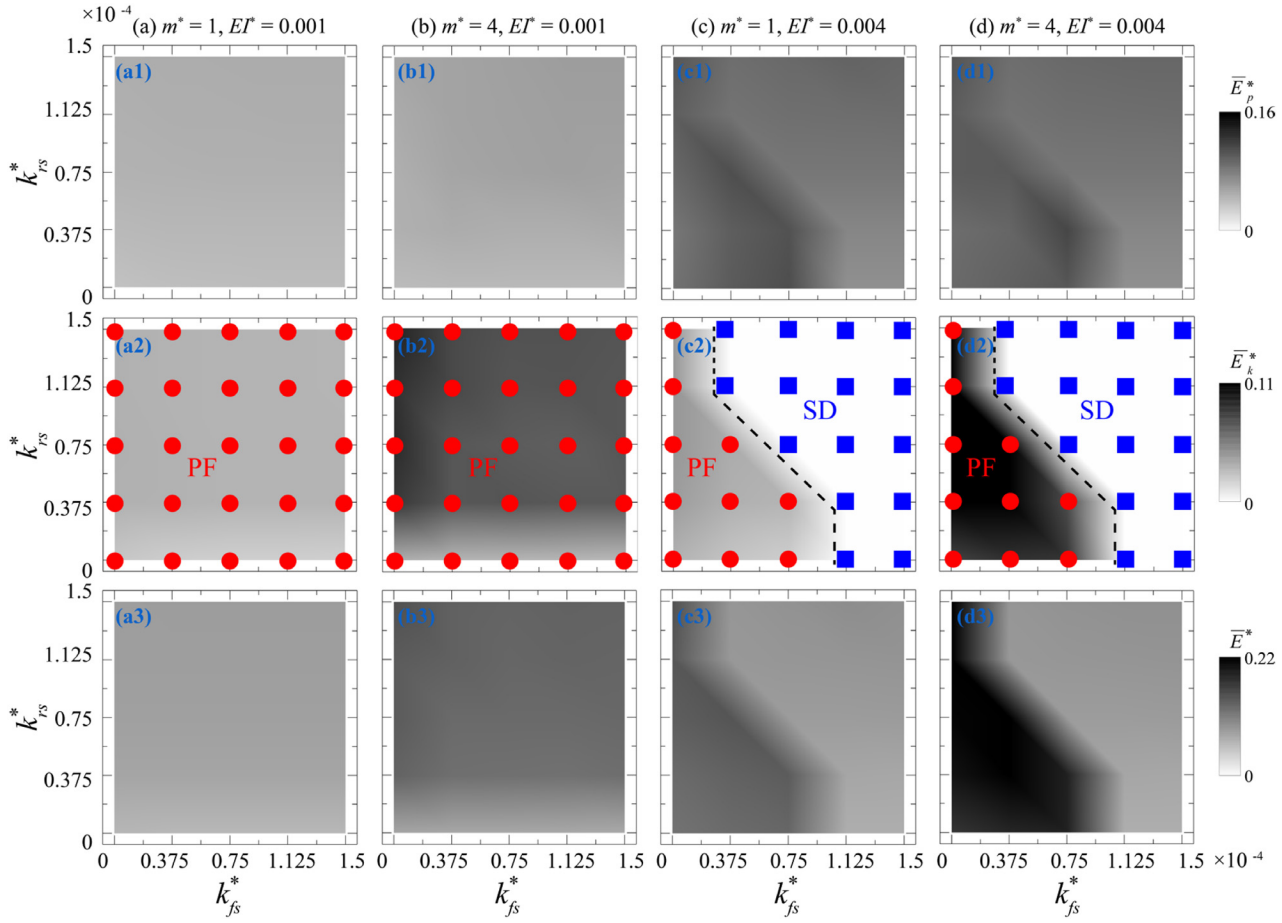

FIG. 20. The effect of the connected spring stiffness on the contours of the time-averaged potential ($\bar{E}_p^*$), kinetic ($\bar{E}_k^*$), and total ($\bar{E}^*$) energies with (a) $m^* = 1$, $EI^* = 0.001$; (b) $m^* = 4$, $EI^* = 0.001$; (c) $m^* = 1$, $EI^* = 0.004$; and (d) $m^* = 4$, $EI^* = 0.004$ at $\Delta L^* = 0.3$. The definition of the red circles and blue squares is identical to Fig. 18. k_{fs}^* denotes the spring flexibility at the front edge, while k_{rs}^* represents the spring flexibility at the back edge.

the case of $k_{fs}^* = 0$, $k_{rs}^* = 1.125 \times 10^{-4}$, with the major difference occurring near the rear edge, as illustrated by the comparable energy values of $k_{rs}^* = 1.125 \times 10^{-4}$ and ∞, and their corresponding energy distribution in Figs. 23(a2)–23(a4) and Figs. 23(b2)–23(b4). In terms of the curvature amplitude, Figs. 23(a1) and 23(b1) show $k_{rs}^* = 1.125 \times 10^{-4}$ considerately lessens the stress concentration at the rear edge, notably in the high-efficient scenario, where the curvature maximum drops from 29.72 to 13.29, reducing by about 55.3% [see Fig. 23(b1)]. Thus, the sheet's safe durability is significantly improved according to the Basquin equation $\lg\sigma_R = a + b\lg N$. This means that retaining a limited stiffness $k_{rs}^* = 1.125 \times 10^{-4}$ can preserve the sheet's efficiency of energy harvesting and concurrently prolong the sheet's fatigue life.

E. Discussion

In this study, we systematically explored the influence of various factors, including boundary conditions, length ratio, bending stiffness, mass ratio, and torsional spring stiffness, on the energy-harvesting performance of a snapping sheet. To offer guidelines for achieving the highest energy efficiency, it is suggested to adopt a front-pinned end and rear-clamped end (0-∞) for the baseline case ($\Delta L^* = 0.1$, $m^* = 1$, and $EI^* = 0.001$). This holds even when the length ratio varies from 0.1 to 0.3, with higher ΔL^* consistently leading to an improved energy-harvesting efficiency. Furthermore, when incorporating the combined effects of bending stiffness (EI^*) and mass ratio (m^*), the 0-∞ case remains the optimal choice. Within the parameter ranges explored, the configuration, characterized by the highest values of $\Delta L^* = 0.3$, $m^* = 4$, and $EI^* = 0.004$, outperforms all the other configurations, with total energy $\bar{E}^*$ achieving approximately 7.06 times that of the baseline case under the same boundary condition. Regarding the influence of the torsional spring, while its inclusion reduces the energy collection to a certain extent, approximately 12.8% in the case of $k_{fs}^* = 0$, $k_{rs}^* = 1.125 \times 10^{-4}$, it enhances the fatigue life of the sheet in a large scale by relieving stress concentration by 55.3%, as demonstrated in Fig. 23(b1).

As for the baseline cases with four different BCs, case 2(0-∞) outperforms the other cases by showing a significantly enhanced kinetic energy and a slightly increased potential energy. These increases are primarily attributable to the reduction in the snapping

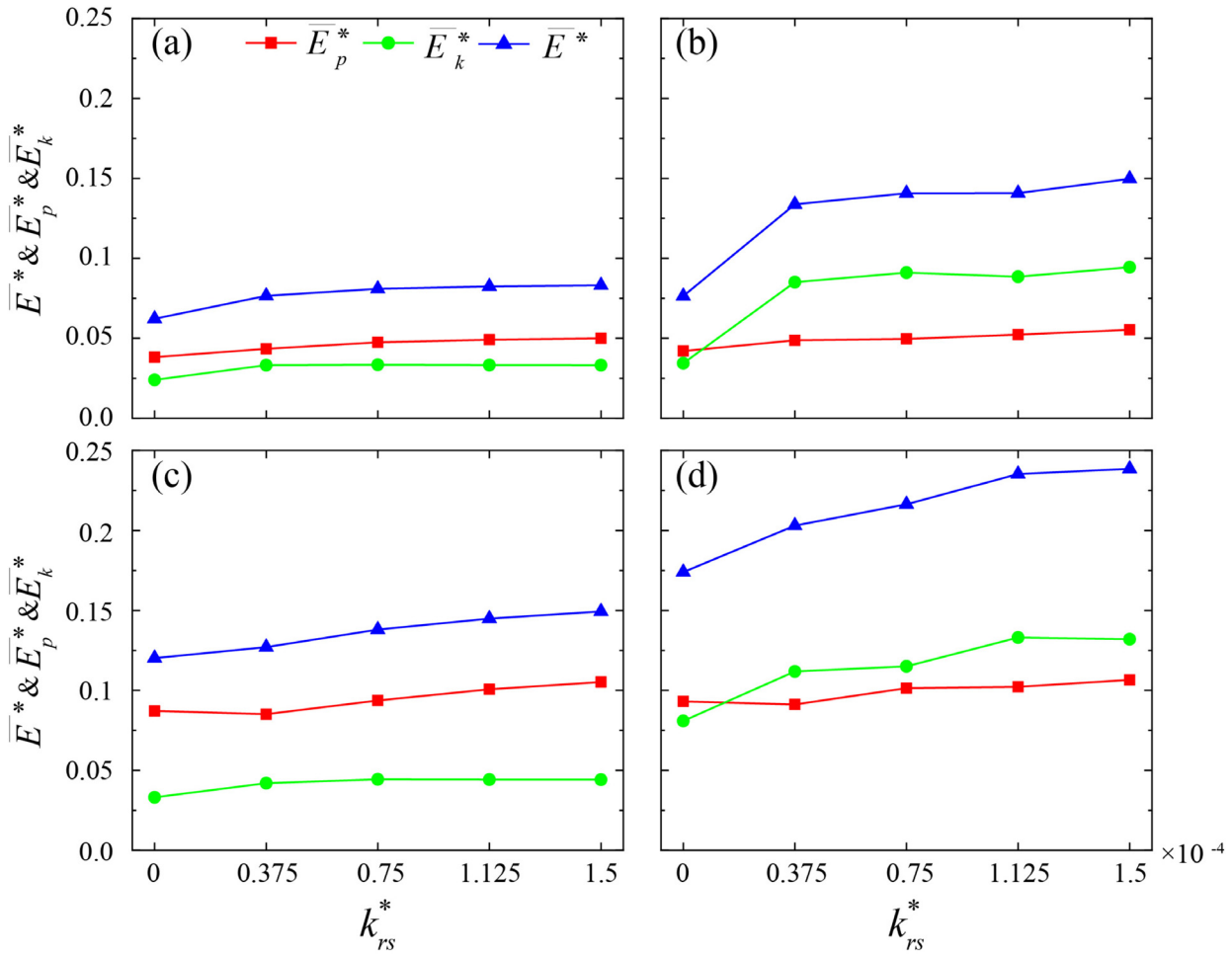

FIG. 21. The effect of the stiffness variations at the rear edge when $k^*_{fs} = 0$ on time-averaged potential ($\bar{E}^*_p$), kinetic ($\bar{E}^*_k$), and total ($\bar{E}^*$) energies with $\Delta L^* = 0.3$: (a) $m^* = 1.0$, $EI^* = 0.001$; (b) $m^* = 4.0$, $EI^* = 0.001$; (c) $m^* = 1.0$, $EI^* = 0.004$; and (d) $m^* = 4.0$, $EI^* = 0.004$.

period and the substantial conversion of potential energy into kinetic energy during the snapping motion, while the increase in potential energy is somewhat counteracted by the relief of the front constraint. In addition, compared to a clamped front end, a pinned-front edge benefits, triggering the sheet's instability to step into a snapping mode. In terms of the ΔL^* effect, increasing the pre-compression of the sheet can remarkably lift the kinetic and potential energies simultaneously, primarily due to the increased curvature and flapping velocity associated with the larger flapping amplitude on the sheet, as shown in Fig. 16. Regarding the energy harvesting along the sheet, the rear portion of the sheet contributes a much larger part. After the snap-through, the sheet entirely deforms upwards with a relatively large velocity distribution (see Figs. 11 and 14), which generates considerable E^*_k. Subsequently, the deformation wave propagates downstream under the fluid force (directed rear-downward), making the rear part fold to a certain extent due to the constraint of the rear edge. The increasing curvature of the sheet's rear section increases the potential energy and hence assists the sheet in achieving its maximum energy harvesting.

Regarding the bending stiffness and the mass ratio, they do improve the energy-harvesting performance when the sheet remains in a periodic flapping mode (see Fig. 18). However, a larger EI^* may lead to a static deflection state, as depicted in cases 3(∞-0) and 4(∞-∞) of Fig. 18. As such, the sheet shifts into a steady state, with the higher bending stiffness canceling out the pressure difference acting on the sheet, resulting in a sudden drop to nearly zero kinetic energy.

IV. CONCLUSIONS

In this study, the effects of BCs on the snapping dynamics and energy-harvesting characteristics of the buckled sheet were numerically studied under different length ratios, bending stiffness, and mass ratios. The following is a summary of the major findings:

(1) The alteration between clamped and pinned BCs significantly affects the sheet's snapping dynamics and energy-harvesting performance. Precisely, the rear clamped end can improve the overall harvested energy evidently by enhancing the potential energy in the rear potion, with the best efficiency achieved in

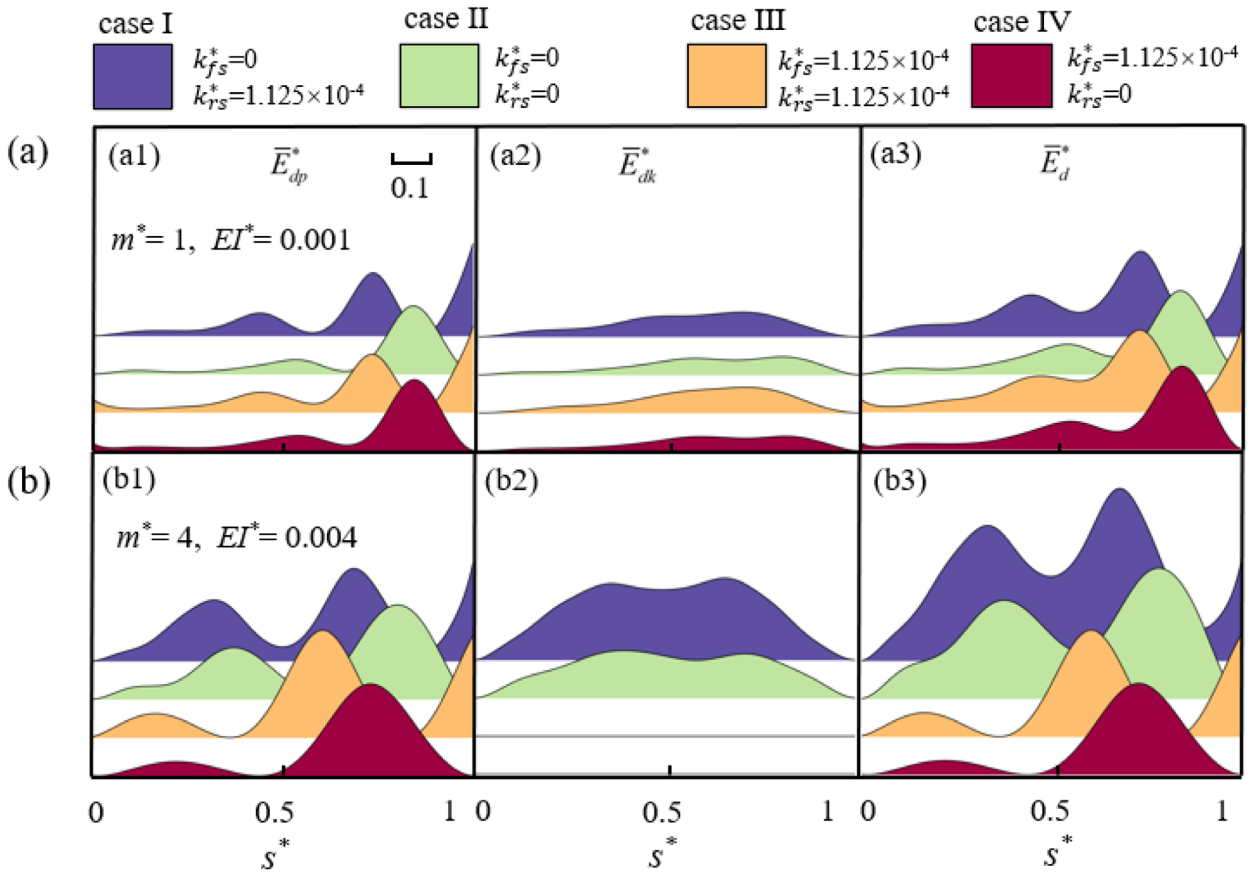

FIG. 22. The superimposed time-averaged energy density distribution along the sheet for the potential ($\bar{E}_{dp}^*$), kinetic ($\bar{E}_{dk}^*$), and total ($\bar{E}_d^*$) energies with $\Delta L^* = 0.3$: (a) $m^* = 1$, $EI^* = 0.001$; (b) $m^* = 4$, $EI^* = 0.004$ at $k_{fs}^* = 0$ and $k_{rs}^* = 1.125 \times 10^{-4}$ (case I), $k_{fs}^* = 0$ and $k_{rs}^* = 0$ (case II), $k_{fs}^* = 1.125 \times 10^{-4}$ and $k_{rs}^* = 1.125 \times 10^{-4}$ (case III), and $k_{fs}^* = 1.125 \times 10^{-4}$ and $k_{rs}^* = 0$ (case IV).

case 2(0-∞). The enhancement of the total energy-harvesting performance is about 61.0% higher than that in case 1(0-0). In contrast, the front-clamped end only slightly affects the energy harvested on the potential portion but triggers a large flapping amplitude than a pinned end.

(2) The energy-harvesting efficiency significantly improves with an increase in length ratio, primarily due to a boost in potential energy gathering. The E_p^* and E_k^* peaks in case 2 increase by about 152.2% and 82.2%, respectively, because of a higher pre-compression ratio. In the whole ΔL^* range (0.1–0.3), the rear clamped end considerably enhances energy extraction, whereas the front end's contribution is minimal, especially in the case of $\Delta L^* = 0.3$.

(3) For all snapping scenarios with different BCs, the energy-harvesting efficiency increases with EI^* and m^* for $\Delta L^* = 0.3$. Compared to the rear end, the front end has far less impact on the energy performance of snapping sheets, especially potential energy. However, the front pinned boundary can more easily excite the sheet's instability when EI^* is considerable, such as $EI^* \geq 0.003$. As a result, it maintains a higher energy-harvesting efficiency than the front-clamped one.

(4) As for the effect of connected elastic springs, it is found that maintaining lower front and rear stiffnesses makes it easier to trigger the sheet's instability, especially when the EI^* is large. The stiffer rear end can achieve a larger improvement on the energy extraction efficiency than the front counterpart, with the sheet at the snapping stage, and this influence becomes essentially stable after certain k_{rs}^*, i.e., 1.125×10^{-4} in the cases of $m^* = 4.0$. It is further found that maintaining a limited k_{rs}^*, i.e., 1.125×10^{-4}, can significantly increase the sheet's fatigue lifetime by reducing the stress concentration while keeping a similar energy-harvesting efficiency with the rear clamped end. But the maximum curvature caused by the stress concentration can be reduced by about 55.3%. It is also noted that the heavier sheet enhances the total energy extraction, primarily by increasing the kinetic energy harvested by the sheet's central portion.

This study provides deeper insights into the effect of BCs on the dynamics and energy-harvesting characteristics of a snapping sheet in uniform flow. However, the impact of sheet's initial shape on its dynamics is worth further in-depth investigation. Nevertheless, deeper investigation, i.e., sensitivity analysis and wave analysis, is needed to

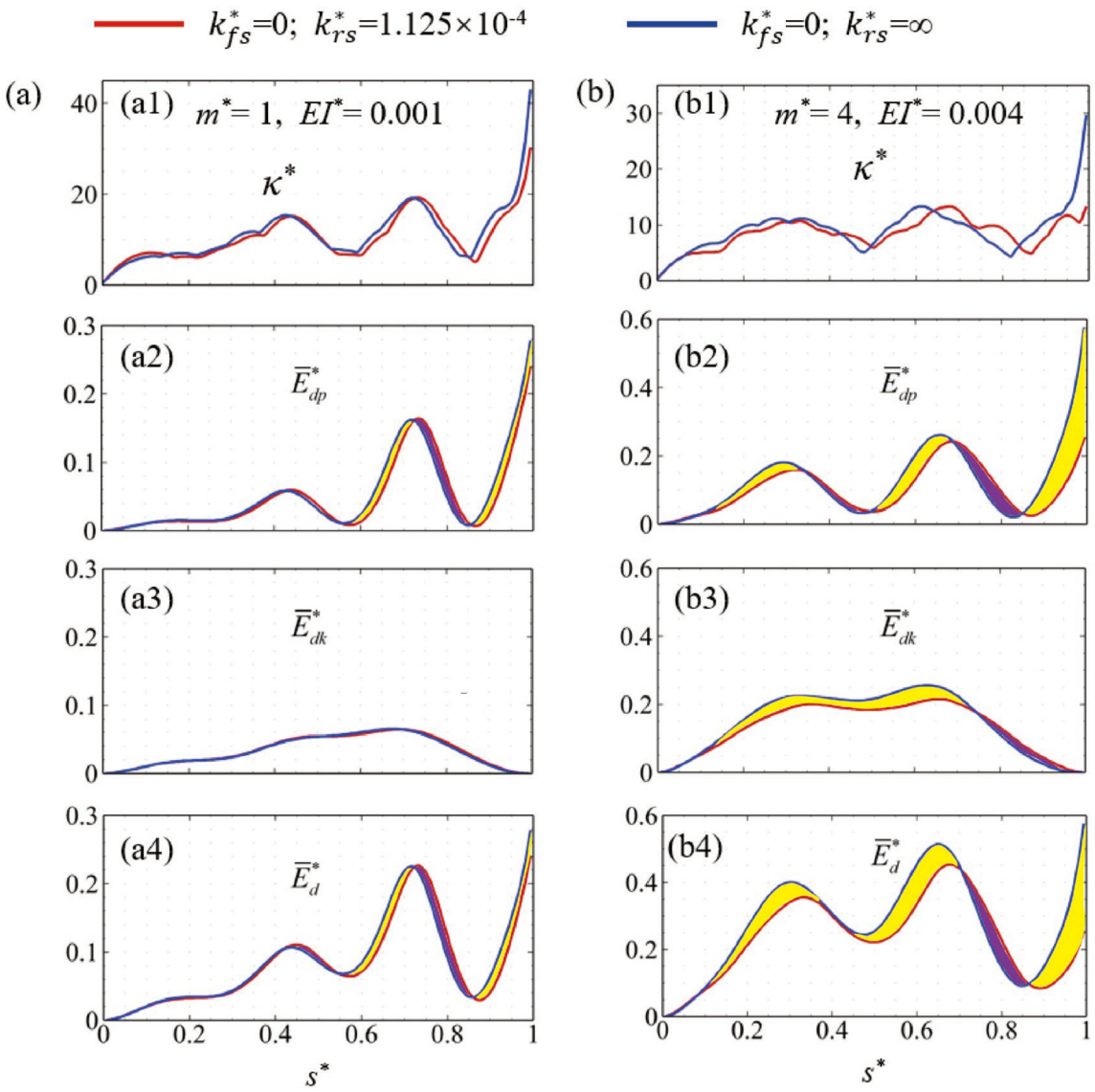

FIG. 23. The curvature amplitude κ^* (first row), time-averaged $\bar{E}_{dp}^*$ (second row), $\bar{E}_{dk}^*$ (third row), and $\bar{E}_d^*$ (fourth row) along the sheet for the scenarios of $k_{fs}^* = 0$, $k_{rs}^* = 1.125 \times 10^{-4}$ and $k_{fs}^* = 0$, $k_{rs}^* = \infty$ at (a) $\Delta L^* = 0.3$, $EI^* = 0.001$, and $m^* = 1$ and (b) $\Delta L^* = 0.3$, $EI^* = 0.004$, and $m^* = 4$. The yellow shows where the rear-end-rigid case ($k_{fs}^* = 0$, $k_{rs}^* = \infty$) over-harvests the energy than that from the rear-end-elastic case ($k_{fs}^* = 0$, $k_{rs}^* = 1.125 \times 10^{-4}$), whereas purple shows under-harvest.

unveil the underlying mechanism of snapping modes' initiation and development. Moreover, the study intends to devise an array of energy harvesters in our future work and evaluate their collective performance for energy harvesting. This will provide a more comprehensive understanding of the potential applications and benefits of this technology.

ACKNOWLEDGMENTS

This work was supported by the Natural Science Foundation of Guangdong Province (Project No. 2021A1515010337) and The Hong Kong Polytechnic University Shenzhen Research Institute (Project No. J2023A011).

AUTHOR DECLARATIONS

Conflict of Interest

The authors have no conflicts to disclose.

Author Contributions

Zhaokun Wang: Conceptualization (equal); Data curation (equal); Methodology (equal); Software (equal); Validation (equal); Writing – original draft (equal); & Writing – review & editing (equal). **Fuwang Zhao:** Formal analysis (equal); Writing – original draft (equal); Writing – review & editing (equal). **Bowen Xu:** Software (equal); Writing – original draft (equal); Writing – review & editing

(equal). **Lingwei Zeng:** Data curation (equal); Formal analysis (equal); Investigation (equal); Software (equal); Supervision (equal); Writing – original draft (equal); Writing – review & editing (equal). **Hui Tang:** Funding acquisition (equal); Project administration (equal); Writing – original draft (equal); Writing – review & editing (equal).

DATA AVAILABILITY

The data that support the findings of this study are available from the corresponding authors upon reasonable request.

REFERENCES

[1]M. M. Alam, L. M. Chao, S. Rehman *et al.*, "Energy harvesting from passive oscillation of inverted foil," Phys. Fluids **33**(7), 075111 (2021).
[2]M. D. A. Al-falahi, S. D. G. Jayasinghe, and H. Enshaei, "A review on recent size optimization methodologies for standalone solar and wind hybrid renewable energy system," Energy Convers. Manage. **143**, 252–274 (2017).
[3]Z. G. Chen, G. Han, L. Yang *et al.*, "Nanostructured thermoelectric materials: Current research and future challenge," Prog. Nat. Sci.: Mater. Int. **22**(6), 535–549 (2012).
[4]S. Amin, "Review on biofuel oil and gas production processes from microalgae," Energy Convers. Manage. **50**(7), 1834–1840 (2009).
[5]Z. K. Wang, F. W. Zhao, Y. Fu *et al.*, "Towards energy harvesting through flow-induced snap-through oscillations," Int. J. Mech. Sci. **254**, 108428 (2023).
[6]H. Li, H. Ren, F. Cao *et al.*, "Improving the galloping energy harvesting performance with magnetic coupling," Int. J. Mech. Sci. **237**, 107785 (2023).
[7]S. Sharma, R. Kiran, P. Azad *et al.*, "A review of piezoelectric energy harvesting tiles: Available designs and future perspective," Energy Convers. Manage. **254**, 115272 (2022).
[8]G. Shi, T. Tan, S. Hu *et al.*, "Hydrodynamic piezoelectric energy harvesting with topological strong vortex by forced separation," Int. J. Mech. Sci. **223**, 107261 (2022).
[9]M. Verma and A. De, "Dynamics of vortex-induced-vibrations of a slit-offset circular cylinder for energy harvesting at low Reynolds number," Phys. Fluids **34**(8), 083607 (2022).
[10]H. X. Pang, A. C. Feng, Y. X. You *et al.*, "Design of novel energy harvesting device based on water flow manipulation," Phys. Fluids **34**(9), 093609 (2022).
[11]M. Mansoor, A. F. Mirza, S. Duan *et al.*, "Maximum energy harvesting of centralized thermoelectric power generation systems with non-uniform temperature distribution based on novel equilibrium optimizer," Energy Convers. Manage. **246**, 114694 (2021).
[12]J. Wang, C. Zhang, M. Zhang *et al.*, "Enhancing energy harvesting from flow-induced vibrations of a circular cylinder using a downstream rectangular plate: An experimental study," Int. J. Mech. Sci. **211**, 106781 (2021).
[13]J. Wang, L. Geng, L. Ding *et al.*, "The state-of-the-art review on energy harvesting from flow-induced vibrations," Appl. Energy **267**, 114902 (2020).
[14]Z. H. Lai, J. L. Wang, C. L. Zhang *et al.*, "Harvest wind energy from a vibro-impact DEG embedded into a bluff body," Energy Convers. Manage. **199**, 111993 (2019).
[15]K. Yu, J. J. Liang, B. Y. Qu *et al.*, "Parameters identification of photovoltaic models using an improved JAYA optimization algorithm," Energy Convers. Manage. **150**, 742–753 (2017).
[16]L. W. Zeng, F. W. Zhao, H. F. Wang *et al.*, "A bi-directional flow-energy harvester," Appl. Phys. Lett. **122**(15), 153901 (2023).
[17]L. W. Zeng, F. W. Zhao, and H. F. Wang, "Control of flow-induced vibration of a circular cylinder using a splitter plate," Phys. Fluids **35**(8), 087104 (2023).
[18]C. L. Wang, H. Tang, and X. Zhang, "Fluid-structure interaction of bio-inspired flexible slender structures: A review of selected topics,"Bioinspiration Biomimetics **17**(4), 041002 (2022).
[19]H. Wang, C. Zhao, L. Zeng *et al.*, "Control of the flow around a finite square cylinder with a flexible plate attached at the free end," Phys. Fluids **34**(2), 27109 (2022).
[20]F. Zhao, M. N. Mumtaz Qadri, Z. Wang *et al.*, "Flow-energy harvesting using a fully passive flapping foil: A guideline on design and operation," Int. J. Mech. Sci. **197**, 106323 (2021).
[21]C. Zhao, H. Wang, L. Zeng *et al.*, "Effects of oncoming flow turbulence on the near wake and forces of a 3D square cylinder," J. Wind Eng. Ind. Aerodyn. **214**, 104674 (2021).
[22]H. Wang, L. Zeng, M. M. Alam *et al.*, "Large eddy simulation of the flow around a finite-length square cylinder with free-end slot suction," Wind Struct. **30**(5), 533–546 (2020).
[23]X. Ma and S. Zhou, "A review of flow-induced vibration energy harvesters," Energy Convers. Manage. **254**, 115223 (2022).
[24]B. Maamer, A. Boughamoura, A. M. R. F. El-Bab *et al.*, "A review on design improvements and techniques for mechanical energy harvesting using piezoelectric and electromagnetic schemes," Energy Convers. Manage. **199**, 111973 (2019).
[25]A. Abdelkefi, "Aeroelastic energy harvesting: A review," Int. J. Eng. Sci. **100**, 112–135 (2016).
[26]J. M. McCarthy, S. Watkins, A. Deivasigamani *et al.*, "Fluttering energy harvesters in the wind: A review," J. Sound Vib. **361**, 355–377 (2016).
[27]F. W. Zhao, Z. K. Wang, M. N. M. Qadri *et al.*, "Effects of wake interaction on energy extraction performance of tandem semi-active flapping foils," Phys. Fluids **35**(8), 087112 (2023).
[28]Y. Zhang, Y. Wang, Y. Xie *et al.*, "Effects of flexibility on energy extraction performance of an oscillating hydrofoil under a semi-activated mode," Energy **242**, 122940 (2022).
[29]V. Mathai, G. A. Tzezana, A. Das *et al.*, "Fluid–structure interactions of energy-harvesting membrane hydrofoils," J. Fluid Mech. **942**, R4 (2022).
[30]V. Joshi and R. C. Mysa, "Mechanism of wake-induced flow dynamics in tandem flapping foils: Effect of the chord and gap ratios on propulsion," Phys. Fluids **33**(8), 087104 (2021).
[31]X. Wu, X. Zhang, X. Tian *et al.*, "A review on fluid dynamics of flapping foils," Ocean Eng. **195**, 106712 (2020).
[32]Z. Liu, F. Tian, J. Young *et al.*, "Flapping foil power generator performance enhanced with a spring-connected tail," Phys. Fluids **29**(12), 123601 (2017).
[33]Q. Xiao and Q. Zhu, "A review on flow energy harvesters based on flapping foils," J. Fluids Struct. **46**, 174–191 (2014).
[34]Q. Zhu, "Optimal frequency for flow energy harvesting of a flapping foil," J. Fluid Mech. **675**, 495–517 (2011).
[35]Z. Peng and Q. Zhu, "Energy harvesting through flow-induced oscillations of a foil," Phys. Fluids **21**(12), 123602 (2009).
[36]M. N. Mumtaz Qadri, F. Zhao, and H. Tang, "Fluid-structure interaction of a fully passive flapping foil for flow energy extraction," Int. J. Mech. Sci. **177**, 105587 (2020).
[37]Z. Liu and H. Qu, "Numerical study on a coupled-pitching flexible hydrofoil under the semi-passive mode," Renewable Energy **189**, 339–358 (2022).
[38]L. Tian, Z. Zhao, W. Wang *et al.*, "Length and stiffness effects of the attached flexible plate on the flow over a traveling wavy foil," Acta Mech. Sin. **37**(9), 1404–1415 (2021).
[39]X. Bai, J. Zhang, J. Zheng *et al.*, "Energy extraction performance of a flapping wing with active elastic airbag deformation at the leading edge," Ocean Eng. **228**, 108901 (2021).
[40]B. Zhu, W. Zhang, and Y. Huang, "Energy extraction properties of a flapping wing with a deformable airfoil," IET Renewable Power Gener. **13**(11), 1823–1832 (2019).
[41]H. Kim, M. Lahooti, J. Kim *et al.*, "Flow-induced periodic snap-through dynamics," J. Fluid Mech. **913**, A52 (2021).
[42]J. Kim, H. Kim, and D. Kim, "Snap-through oscillations of tandem elastic sheets in uniform flow," J. Fluids Struct. **103**, 103283 (2021).
[43]H. Kim, Q. Zhou, D. Kim *et al.*, "Flow-induced snap-through triboelectric nanogenerator," Nano Energy **68**, 104379 (2020).
[44]W. Qin, W. Deng, J. Pan *et al.*, "Harvesting wind energy with bi-stable snap-through excited by vortex-induced vibration and galloping," Energy **189**, 116237 (2019).
[45]N. Hu and R. Burgueño, "Buckling-induced smart applications: Recent advances and trends," Smart Mater. Struct. **24**(6), 063001 (2015).
[46]D. N. Betts, H. A. Kim, C. R. Bowen *et al.*, "Optimal configurations of bistable piezocomposites for energy harvesting," Appl. Phys. Lett. **100**(11), 114104 (2012).
[47]K. Tan, L. Chen, S. Yang *et al.*, "Dynamic snap-through instability and damped oscillation of a flat arch of hard magneto-active elastomers," Int. J. Mech. Sci. **230**, 107523 (2022).

[48]R. Badhurshah, R. Bhardwaj, and A. Bhattacharya, "Lock-in regimes for vortex-induced vibrations of a cylinder attached to a bistable spring," J. Fluids Struct. **91**, 102697 (2019).
[49]Y. Zhu and J. W. Zu, "Enhanced buckled-beam piezoelectric energy harvesting using midpoint magnetic force," Appl. Phys. Lett. **103**(4), 41905 (2013).
[50]F. Cottone, L. Gammaitoni, H. Vocca *et al.*, "Piezoelectric buckled beams for random vibration energy harvesting," Smart Mater. Struct. **21**(3), 035021 (2012).
[51]B. S. H. Connell and D. K. P. Yue, "Flapping dynamics of a flag in a uniform stream," J. Fluid Mech. **581**, 33–67 (2007).
[52]C. Wang and H. Tang, "On the aeroelastic energy transfer from a Lamb dipole to a flexible cantilever," J. Fluids Struct. **86**, 170–184 (2019).
[53]R. Hua, L. Zhu, and X. Lu, "Locomotion of a flapping flexible plate," Phys. Fluids **25**(12), 121901 (2013).
[54]T. Krüger, H. Kusumaatmaja, A. Kuzmin *et al.*, *The Lattice Boltzmann Method* (Springer International Publishing, 2017).
[55]Z. Guo and C. Shu, *Lattice Boltzmann Method and Its Application in Engineering* (World Scientific, 2013).
[56]L. S. Luo, W. Liao, X. Chen *et al.*, "Numerics of the lattice Boltzmann method: Effects of collision models on the lattice Boltzmann simulations," Phys. Rev. E **83**(5), 56710 (2011).
[57]Z. Guo, C. Zheng, and B. Shi, "Discrete lattice effects on the forcing term in the lattice Boltzmann method," Phys. Rev. E **65**(4 Pt. 2B), 046308 (2002).
[58]P. Lallemand and L. S. Luo, "Theory of the lattice Boltzmann method: Dispersion, dissipation, isotropy, Galilean invariance, and stability," Phys. Rev. E **61**(6 Pt. A), 6546–6562 (2000).
[59]X. He, Q. Zou, L. Luo *et al.*, "Analytic solutions of simple flows and analysis of nonslip boundary conditions for the lattice Boltzmann BGK model," J. Stat. Phys. **87**(1–2), 115–136 (1997).
[60]A. Mohamad, *Lattice Boltzmann Method* (Springer, 2011).
[61]Z. L. Guo, C. G. Zheng, and B. C. Shi, "Non-equilibrium extrapolation method for velocity and pressure boundary conditions in the lattice Boltzmann method," Chin. Phys. **11**(4), 366 (2002).
[62]M. Schulz and F. C. Filippou, "Non-linear spatial Timoshenko beam element with curvature interpolation," Int. J. Numer. Methods Eng. **50**(4), 761–785 (2001).
[63]J. F. Doyle, *Nonlinear Analysis of Thin-Walled Structures: Statics, Dynamics, and Stability* (Springer Science & Business Media, 2001).
[64]M. A. Crisfield, "A consistent co-rotational formulation for non-linear, three-dimensional, beam-elements," Comput. Methods Appl. Mech. Eng. **81**(2), 131–150 (1990).
[65]Z. K. Wang, C. L. Wang, F. W. Zhao *et al.*, "Simulation of fluid-structure interaction during the phaco-emulsification stage of cataract surgery," Int. J. Mech. Sci. **214**, 106931 (2022).
[66]C. S. Peskin, "The immersed boundary method," Acta Numer. **11**, 479–517 (2002).
[67]W. Huang, S. J. Shin, and H. J. Sung, "Simulation of flexible filaments in a uniform flow by the immersed boundary method," J. Comput. Phys. **226**(2), 2206–2228 (2007).
[68]A. A. Delouei, M. Nazari, M. H. Kayhani *et al.*, "Direct-forcing immersed boundary–non-Newtonian lattice Boltzmann method for transient non-isothermal sedimentation," J. Aerosol Sci. **104**, 106–122 (2017).
[69]S. K. Kang, *Immersed Boundary Methods in the Lattice Boltzmann Equation for Flow Simulation* (ProQuest Dissertations Publishing, 2010).
[70]S. P. Timoshenko and J. M. Gere, *Theory of Elastic Stability* (Courier Corporation, 2009).
[71]I. Lee and H. Choi, "A discrete-forcing immersed boundary method for the fluid–structure interaction of an elastic slender body," J. Comput. Phys. **280**, 529–546 (2015).
[72]M. D. de Tullio and G. Pascazio, "A moving-least-squares immersed boundary method for simulating the fluid–structure interaction of elastic bodies with arbitrary thickness," J. Comput. Phys. **325**, 201–225 (2016).
[73]K. A. Zakaria, S. Abdullah, M. J. Ghazali *et al.*, "A review of the loading sequence effects on the fatigue life behaviour of metallic materials," J. Eng. Sci. Technol. Rev. **9**(5), 189–200 (2016).
[74]T. Nicholas, *High Cycle Fatigue: A Mechanics of Materials Perspective* (Elsevier, 2006).
[75]A. D'Amore, G. Caprino, P. Stupak *et al.*, "Effect of stress ratio on the flexural fatigue behaviour of continuous strand mat reinforced plastics," Sci. Eng. Compos. Mater. **5**(1), 1–8 (1996).
[76]H. E. Boyer, *Atlas of Fatigue Curves* (ASM International, 1985).
[77]Y. B. Liu, Y. D. Li, S. X. Li *et al.*, "Prediction of the S–N curves of high-strength steels in the very high cycle fatigue regime," Int. J. Fatigue **32**(8), 1351–1357 (2010).
[78]Y. Mao, S. Zhong, and H. Yin, "Active flow control using deep reinforcement learning with time delays in Markov decision process and autoregressive policy," Phys. Fluids **34**(5), 53602 (2022).